

AN ABSTRACT OF THE THESIS OF

Shalu Bansal for the degree of Master of Science in Material Science presented on June 30, 2017

Title: An Investigation on Nanoscale-shape-mediated Coupling Between Temperature and Densification in Intense Pulsed Light Sintering of Silver Nanoparticles

Abstract Approved:

Rajiv Malhotra

In Intense Pulsed Light (IPL) sintering, pulsed large-area visible light from a xenon lamp is absorbed by nanoparticle films or patterns and converted to heat, resulting in rapid sintering of the nanoparticles. This work experimentally characterizes IPL sintering of silver nanoparticle films. A newly observed turning point in the evolution of film temperature during IPL sintering is correlated to the observation, in literature and in this work, that film densification levels off beyond a critical pulse fluence and number of pulses. A computational model is developed that couple electromagnetic finite element analysis, heat transfer models and densification models to predict the evolution of film temperature and density during IPL. This model is able to capture the experimentally observed turning point in temperature during IPL, whereas current models of IPL are

unable to do so. It is shown that the temperature turning point occurs due to a coupling between optical absorption and densification in the nanoparticle film, mediated by a change in nanoscale shape of the deposited nanoparticles due to interparticle neck growth. Further, it is found that the optical fluence per pulse has a greater effect on the achievable film density in IPL, as compared to the number of pulses.

© Copyright by Shalu Bansal

June 30, 2017

All Rights Reserved

An Investigation on Nanoscale-shape-mediated Coupling Between Temperature and
Densification in Intense Pulsed Light Sintering of Silver Nanoparticles

by

Shalu Bansal

A THEIS

submitted to

Oregon State University

in partial fulfilment of

the requirements for the

degree of

Master of Science

Presented June 30, 2017

Commencement June 2018

Master of Science thesis of Shalu Bansal presented on June 30, 2017.

Approved:

Major Professor representing Material Science

Head of the School of Mechanical, Industrial and Manufacturing Engineering

Dean of the Graduate School

I understand that my thesis will become part of the permanent collection of Oregon State University libraries. My signature below authorizes release of my thesis to any reader upon request.

Shalu Bansal, Author

ACKNOWLEDGEMENTS

I would like to express gratitude towards my advisor for giving me opportunities to develop research skills for experiments and modelling aspect. I am indebted for his guidance and assistance in writing papers and modelling efforts for this work.

I am thankful to Dr. Chih-hung Chang and his research group for usage of several tools in their lab. I appreciate collaboration with Zhongwei Gao and providing me with thin film samples needed for my research. I would also like to thank Teresa Sawyer for educating me about the nuances of electron microscopy and Neil Thorton for training me on the equipment at ATAMI needed for my projects. Further, I gratefully acknowledge the financial support from the National Science Foundation to carry out this research.

I would like to thank my colleagues especially Will, Hank, Roshan and Michael at AMPL lab for their assistance in construction of the wooden enclosure for the IPL equipment and other stuff needed for my research. Also, it would be difficult to survive without Ali's stress-relieving jest and Kelli's cookies.

Finally, I acknowledge Abhishek for inspiring and supporting me during the pursuit and completion of this thesis. My parents and siblings for their love and affection throughout my life.

TABLE OF CONTENTS

	<u>Page</u>
1 Introduction	1
1.1 Motivation	1
1.2 Existing Methods – Comparison: IPL vs other method	3
1.3 Literature Review	5
1.4 Challenges	8
1.5 Goals.....	8
2 Experiments and Modelling Methods.....	10
2.1 Experimental methods.....	10
2.1.1 Film preparation:.....	10
2.1.2 IPL setup and parameters used:	11
2.1.3 Film characterization:	12
2.2 Computational Modeling.....	13
2.2.1 Nanoscale Model:	14
2.2.2 Mesoscale Model:	20
3 Results and Discussion	26
3.1 Experimental Results.....	26
3.1.1 Temperature evolution	26

TABLE OF CONTENTS (continued)

	<u>Page</u>
3.1.2 Morphological change	27
3.1.3 Particle size and Sheet Resistance	33
3.2 Predictions from Modeling.....	36
4 Conclusions and Future work	47
Bibliography	50

LIST OF FIGURES

<u>Figure</u>	<u>Page</u>
Figure 1.1: Schematic for application of porous thin film devices: (a) Semiconducting oxide as gas sensing element in gas sensor [18] (b) ZnO layer for photocatalysis[19] (c) Design structure for dielectric capacitor [20]	1
Figure 1.2: Application for dense thin films in (a) Photovoltaics (b) RFID (c) flexible displays	2
Figure 1.3: Working principle of IPL	6
Figure 2.1: Measured size distribution of Ag nanoparticles of (a) Nominal diameter 20 nm, measured mean diameter = 19.5 nm, standard deviation = 6 nm. Length scale in inset TEM image is 50 nm (b) Nominal diameter 40 nm, measured mean diameter = 39.8 nm, standard deviation = 4 nm	10
Figure 2.2: Experimental setup for IPL sintering	11
Figure 2.3. Measured emissivity as a function of number of IPL pulses and pulse fluence for (a) 20 nm and (b) 40 nm Ag nanoparticle films	13
Figure 2.4: Schematic of (a) COMSOL FEA for an ensemble of five Ag nanoparticles (b) two unequal size nanoparticles with the relevant geometrical parameters used in the nanoscale sintering model (c) Ag nanoparticle layers used in COMSOL FEA.	14
Figure 2.5: Spectral output of the Sinteron 3000 IPL system.....	17
Figure 2.6: Predicted thermal power per unit incident optical power, i.e., Q_{λ} , for Ag nanoparticle ensembles shown in figure 2.4 a with nanoparticle diameters (a) 20 nm (b) 40 nm.	19
Figure 2.7: Schematic of the mesoscale model (dimensions not to scale).....	20
Figure 2.8: Effect of activation energy E_{act} on predicted temperature evolution as compared to experimental evolution of temperature for fluence E2 on 20 nm Ag nanoparticle film.	24
Figure 3.1: Temperature evolution over 150 pulses during IPL of 20 nm diameter nanoparticle films at fluence (a) E1 (b) E2 (c) E3; and during IPL of 40 nm films at fluence (d) E1 (e) E2 (f) E3.	27

LIST OF FIGURES (continued)

<u>Figure</u>	<u>Page</u>
Figure 3.2: Planar SEM micrographs of 20 nm Ag film (a) unsintered; and sintered with 150 IPL pulses at fluence (b) E1 (c) E2 (d) E3. Cross-sectional SEM images of 20 nm Ag film near substrate for 150 IPL pulses at fluence (e) E1 (f) E2 (g) E3. Larger scale planar SEM micrographs for 20 nm Ag film (h) unsintered (i) sintered at fluence E1 (j) sintered at fluence E2 (k) sintered at fluence E3.	29
Figure 3.3: SEM micrographs of 40 nm Ag film (a) unsintered; and sintered with 150 IPL pulses at fluence (b) E1 (c) E2 (d) E3. Cross-sectional SEM images of 40 nm Ag film near substrate for 150 IPL pulses at fluence (e) E1 (f) E2 (g) E3.....	30
Figure 3.4: SEM micrographs of 40 nm Ag nanoparticle films (a) unsintered; and IPL sintered with (b) E1-150 pulses (c) E2-50 pulses (d) E2-90 pulses (e) E2-150 pulses (f) E3-50 pulses (g) E3-90 pulses (h) E3-150 pulses.....	31
Figure 3.5: Larger scale planar SEM micrographs for 40 nm Ag film (a) unsintered (b) sintered at fluence E1 (c) sintered at fluence E2 (d) sintered at fluence E3.	32
Figure 3.6: Representative XRD curves for unsintered and sintered 20 nm Ag nanoparticle film, as a function of number of pulses, for fluence E3.....	33
Figure 3.7: Change in particle size with number of pulses and fluence for (a) 20 nm Ag film (b) 40 nm Ag film. Error bars show standard deviation in measured particle size. Change in Ag (111) peak intensity with number of pulses and fluence for (c) 20 nm Ag film (d) 40 nm Ag film. Change in FWHM at Ag (111) peak with number of pulses and fluence for (e) 20 nm Ag film (f) 40 nm Ag film. Change in sheet resistance with number of pulses and fluence for (g) 20 nm Ag film (g) 40 nm Ag film.	35
Figure 3.8: (a) Representative predicted contours of volumetric thermal power dissipation in W/m^3 as a function of neck size x , for 20 nm Ag nanoparticles at $\lambda = 400$ nm; (b) Representative predicted contours of volumetric thermal power dissipation in W/m^3 for multilayered unsintered nanoparticle ensemble of 20 nm Ag nanoparticles, at $\lambda = 400$ nm; (c) Predicted function $Q_s(\theta)$; (d) Predicted function $Q_s(z)$. All results shown for 1 V/m incident electric field.....	38
Figure 3.9: Temperature predictions by coupled and uncoupled models compared to experimentally measured temperature for fluence (a) E3 (b) E2 (c) E1; and (d) Predicted volume fraction, for 20 nm Ag nanoparticle film.	40
Figure 3.10: Temperature predictions by coupled and uncoupled models compared to experimentally measured temperature for fluence (a) E3 (b) E2 (c) E1; and (d) Predicted volume fraction, for 40 nm Ag nanoparticle film.	41

LIST OF FIGURES (continued)

<u>Figure</u>	<u>Page</u>
Figure 3.11: Effect of varying fluence and number of pulses on predicted (a) film temperature (b) solid volume fraction, for 20 nm Ag nanoparticle film.	44
Figure 3.12: Effect of varying fluence and number of pulses on predicted (a) film temperature (b) solid volume fraction, for 40 nm Ag nanoparticle film.	45

1 Introduction

1.1 Motivation

Thin films find widespread application in electronic devices[1], energy generation, harvesting[2] and storage, sensors and catalysis[3]. These applications include thin film transistor(TFT)[4], radio-frequency identification(RFID) tags[5], memory devices[6,7], lighting and flexible displays[8]; solar cells[9], fuel cells[10], batteries[11], supercapacitors[12,13]; sensors for physiological[14,15] and environmental monitoring[16]. Such thin films, either as printed patterns or as contiguous films, have been employed to build above devices with dense or porous morphology[17] on large area rigid or flexible substrates such as glass, plastics films, metallic foil, and fibrous materials (like paper, textile and biological substrate). Figure 1.1 and Figure 1.2 illustrate a few examples of thin film applications.

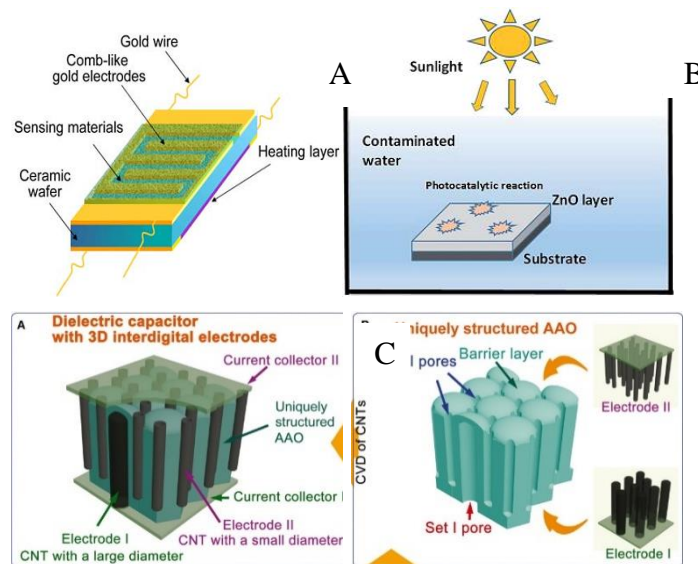


Figure 1.1: Schematic for application of porous thin film devices: (a) Semiconducting oxide as gas sensing element in gas sensor [18] (b) ZnO layer for photocatalysis[19] (c) Design structure for dielectric capacitor [20]

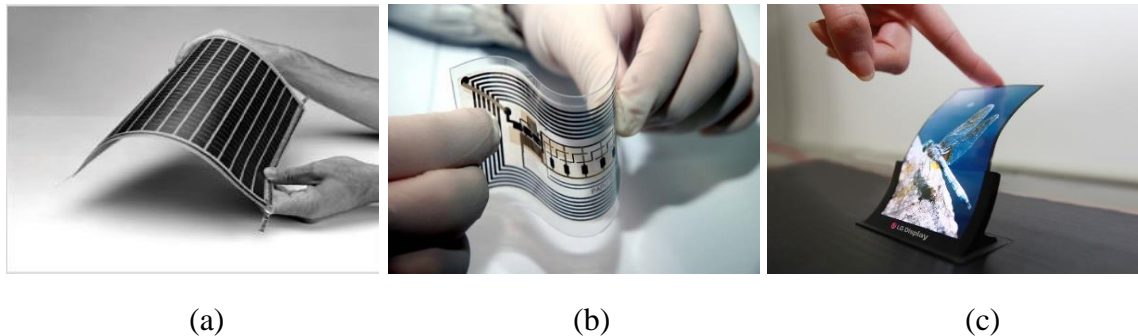


Figure 1.2: Application for dense thin films in (a) Photovoltaics (b) RFID (c) flexible displays

A variety of nanomaterials are employed for these thin film devices including metals and semiconductors. Metal nanoparticles and nanowires are used for conductive contacts, interconnects and as TCO (transparent conductive material) for flexible and stretchable electronic devices [21]. Semiconductors such as halide perovskites[22] and metal chalcogenides[23,24] like CdTe, CZTS, CIGS are used in thin film solar cells as photoabsorber layer. Further, semiconducting oxides[18,25] like SnO₂, ZnO, TiO₂, IGZO(In-Ga-Zn oxide), ITO thin films forms the building block for sensor, catalysis and displays.

Recently, thin film fabrication is carried out by continuous, additive manufacturing processes[26] utilizing solution based routes which offers a scalable, low cost alternative to conventional vacuum based process. A typical process involves contact/non-contact printing or deposition of film at ambient temperature and pressure conditions using nanoparticle solution based ink. In addition, a thermal treatment or sintering[27] is often required as post–deposition/printing step for enhancing the properties of these thin films to

its functionalities. Roll to Roll technology (R2R) is one such technology at industrial platform offering high throughput and cost-efficiency for thin film fabrication. Further, use of heat sensitive material such as flexible polymeric substrates for fabrication of flexible electronics necessitates processing below glass transition temperature T_g to minimize their thermal damage and distortion. Hence, short sintering times and low sintering temperature are bottleneck for compatibility of sintering step with R2R.

Sintering involves coalescence of particles to cause densification on application of either heat and/or pressure below melting temperature. The driving force for sintering is elimination of surface area by neck formation between adjacent particles via inter-diffusion of atoms. Nanomaterials has large specific surface energy (due to high surface to volume ratio) and lower melting points enhancing the surface diffusion while minimizing the energy requirements for sintering[28]. Hence, sintering at nanoscale requires relatively lower temperature than at micro/macro scale. Further, controlling porosity[17,18] while retaining its nanosize features through sintering is essential to obtain desired microstructure morphology and functionalities for certain applications like catalysis and sensing. Therefore, it is essential to understand the correlation between nanomaterial size/shape, sintering temperatures, sintering process times, functional properties of deposited films and their microstructure morphology.

1.2 Existing Methods – Comparison: IPL vs other method

Conventionally, nanoparticle sintering can be implemented via thermal sintering in an oven or a hot plate for metals and ceramics. However, this process suffers from long sintering time (~ several minutes to few hours) and high processing temperature (>150-

200 C) makes it incompatible for R2R manufacturing and flexible substrate. Alternative sintering methods such as microwave[29], electrical[30], low pressure argon plasma[31], chemical [32] or photonic (electromagnetic irradiation ranging UV to visible to IR spectrum)[33] sintering has been demonstrated in literature which can considerably reducing the processing temperature and time relative to thermal sintering. Table 1.1 presents a comparison of the existing sintering process.

Table 1.1: Comparison of existing sintering method

Sintering Method	Operates in	Equip. Cost	Material Capability	Time	Scalability	Polymer substrate
Furnace	Chamber	\$\$	High	Slow	**	No
Microwave	Chamber	\$\$	Medium	Moderate	*	Yes
Electrical	Ambient	\$	Low	Fast	*	Yes
Laser	Ambient	\$\$\$	Medium	Moderate	**	Yes
IPL	Ambient	\$\$	High	Fast	***	Yes

Microwave sintering[29] is used for dielectric and conductive material reducing the sintering time to few minutes. However, its efficiency is limited by the penetration depth (ex- 1.3 μm for silver at 2.54 GHz frequency[29]) into the nanomaterial causing non-uniform heating while operating in a closed microwave chamber. Electrical sintering[30] employs resistive Joule heating (or ohmic heating) of conductive material for sintering with advantages of short sintering time (in seconds) and reduced substrate heating. This process, however, is limited by its applicability to conductive material with often requirement of a

thermal pre-sintering step[34]. Plasma sintering[31] involves interaction of high energy plasma species in a vacuum chamber for its operation with long processing time. Chemical sintering involves exposures to vapor. All these processes except photonic sintering method have limited compatibility with R2R process[34,35].

Laser sintering, infrared (IR) sintering and intense pulse light (IPL) sintering are non-contact, photonic sintering processes. They provide high energy photons in short duration which are selective absorbed by nanomaterial to cause heating and sintering without affecting the underlying thermally sensitive substrate. In laser sintering, each metallic nanoparticles require a single wavelength elevating the cost. In contrast, IPL uses broad spectrum enabling wide material range for sintering. Further, laser sintering [36] is carried out by a small spot source size using raster scan method making it a relatively slower process. IPL uses pulsed light from xenon lamp to sinter over large area. With the increasing demand of large area and low temperature processing for flexible polymer substrate, IPL sintering is a promising technique.

As discussed, there is a need for a sintering process with the following characteristics to meet the requirements for scalable thin film manufacturing:

- Low temperature processing
- Large sintering area and shorter processing time
- Capable of handling a wide range of materials- metals and semiconductor
- Controllable density, morphology and functionality

1.3 Literature Review

In Intense Pulsed Light Sintering (IPL), visible (400-700 nm), pulsed light from a xenon lamp is delivered over large-area (upto 9 sq. inches or greater optical footprint). This light is absorbed and converted into heat by nanoparticles deposited on a substrate, resulting in densification of the nanoparticles as shown in Figure 1.3.3. Faster densification (within seconds) over larger areas gives IPL a significant advantage over conventional nanoparticle sintering processes like oven-based[37] and laser-based sintering[36]. The capability of IPL to sinter metallic (Cu [38,39], Ag[40–42], Ni [43]) and non-metallic (e.g., CIGS[44], CdTe[45], CdS [45], CZTS[46]) nanoparticles for applications in printed electronics, solar cells, gas sensing and photocatalysis has been demonstrated.

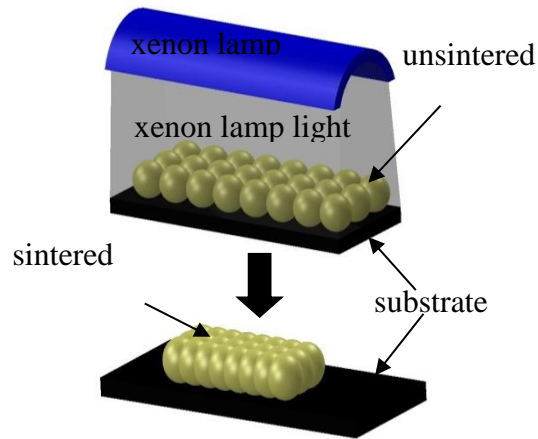


Figure 1.3: Working principle of IPL

Metallic nanomaterial can be locally heated at the interface when optically illuminated due to LSPR (localized surface plasmonic resonance) causing photo-thermal effects[47]. Heat generation is a function of its absorption cross-section, its shape/size/distribution, surrounding medium and wavelength and irradiance of the incoming light[48].

Past experimental work on IPL of metallic nanoparticles[36,41,49] has shown that nanoparticle densification begins above a critical optical fluence per pulse, after which the density rises with greater fluence and number of pulses. The above works also show that for a constant fluence, there is a critical number of pulses beyond which there is very little additional increase in densification, i.e., the densification levels off. This leveling off in densification occurs despite no change in the optical energy from the xenon lamp, and in spite of the fact that densification in the film is not complete (as seen in Scanning Electron Microscopy images of the sintered film). Due to the absence of external pressure in IPL the densification of nanoparticles of the same size, same material and deposited using the same method as in the aforementioned works, depends primarily on the temperature history of the nanoparticle film. Thus, understanding and predicting evolution of film temperature during IPL is critical to understanding the evolution of density in the IPL process.

West et al.[50] used a heat transfer model based on experimentally measured optical absorption by the unsintered nanoparticle film, effective medium theory, and known optical power from the xenon lamp, to model the evolution of film temperature during IPL of Ag nanoparticle films. Lavery et al.[51] and Kim et al. [38] developed similar thermal Finite Element Analysis (FEA) models to predict temperature evolution and melting during IPL of perovskite and Cu nanoparticles respectively. However, these works did not compare predicted and experimentally measured temperature evolution during IPL.

More recent modeling efforts [33,52] based on a similar approach have predicted temperatures that compare favorably to those seen in experiments on IPL of Cu nanoparticles. As a result, these models predict either the absence of occurrence of melting

in the nanoparticle film, which is a conservative measure of densification. Further, optically welding of silver nanowires has been show

1.4 Challenges

Based on the above literature review, the following key challenges can be identified:

- Leveling off in densification and its correlation with the sintering temperature is not explored during IPL
- Neck growth between the nanoparticles is not modeled during IPL
- Comparison between the simulations predicted and experimentally measured temperature evolution during IPL
- IPL parameters to control the densification and film properties.

1.5 Goals

This work[53] aims to understand the following:

- Experiments are conducted to characterize the evolution of temperature, microstructural morphology and crystallinity of the nanoparticle film as a function of the fluence, number of pulses and nominal nanoparticle size during IPL.
- Experimentally turning point in evolution of film temperature is observed and is correlated to the experimentally observed leveling off in nanoparticle densification in the film.
- A computational model is developed, that links electromagnetic FEA of optical energy absorption and semi-analytical models of interparticle neck growth in nanoparticle ensembles, to mesoscale transient heat transfer and densification. It is

shown that this model captures the experimentally observed temperature turning point in IPL, whereas current models of IPL are unable to do so.

In this work, silver nanoparticles is used due to its application in conductive films owing to their oxidation resistance and low resistivity. Further, the developed model is used to show that the temperature turning point in IPL is due to a change in the nanoscale shape of the deposited nanoparticles due to interparticle neck growth, via which the nanoscale optical absorption and densification are coupled to each other. This coupling phenomenon is the source of the observation of a temperature turning point during IPL. The developed model is further used to show that fluence has a greater effect on the achievable film density in IPL, as compared to the number of pulses. The implications of these observations on enhanced control of the IPL process are also discussed.

2 Experiments and Modelling Methods

2.1 Experimental methods

2.1.1 Film preparation:

Commercially obtained Ag nanoparticles (US Research Nanomaterial Inc.) of nominal size 20 nm and 40 nm were dissolved in tetradecane at 48% by weight without any dispersant. Figures 2.1a and 2.1b show the size distribution of the nanoparticles as measured by TEM. After ultrasonication for one hour the inks were found to stay in solution for at least a 24 hour period, during which experiments were conducted. The inks were spin-coated on to a 250 μm thick Kapton substrate and dried at room temperature. The nominal film thickness measured using a ZeScope white light interferometer (resolution 300 nm) was 10 μm over a 25 mm x 25 mm area.

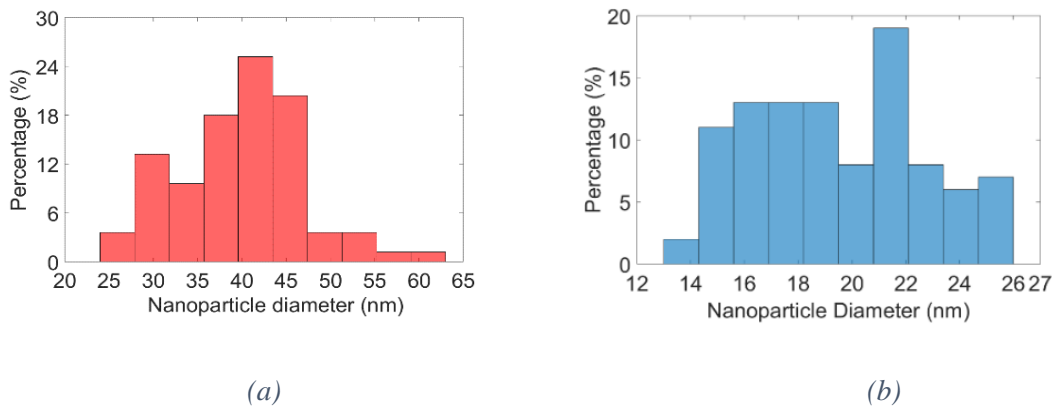


Figure 2.1: Measured size distribution of Ag nanoparticles of (a) Nominal diameter 20 nm, measured mean diameter = 19.5 nm, standard deviation = 6 nm. Length scale in inset TEM image is 50 nm (b) Nominal diameter 40 nm, measured mean diameter = 39.8 nm, standard deviation = 4 nm

2.1.2 IPL setup and parameters used:

IPL was performed using a Sinteron 3000 system (Xenon Corporation) consisting of a linear xenon lamp with an elliptical reflector that focusses light to a rectangular optical footprint of 12 inches by 1.75 inches at a focal distance of 1.0 inch from the surface of the lamp. In this system, the on-time t_{on} (in microseconds) and the lamp voltage V (in volts) are used to control the optical energy per pulse E_p as per the relationship $E_p = (V/3120)^{2.4} \times t_{on}$.

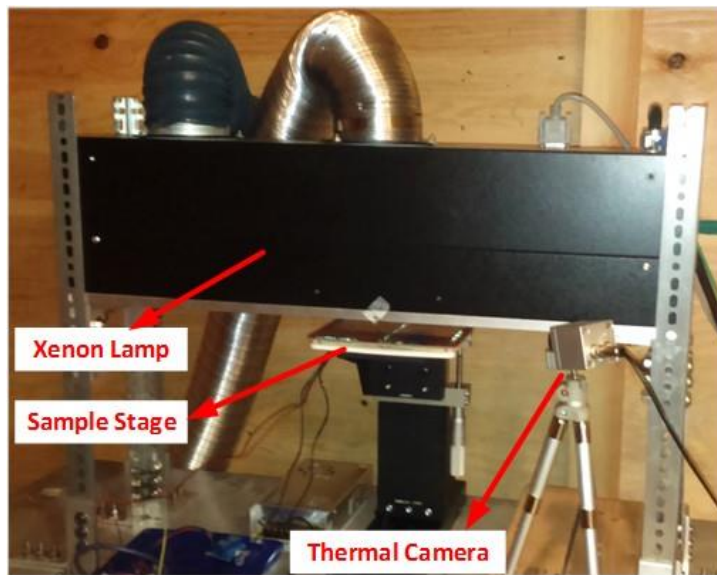


Figure 2.2: Experimental setup for IPL sintering

The spin-coated Kapton samples were placed on borosilicate glass on a sample holder platform, which was mounted onto a micrometer stage, such that the coated Kapton was at a distance of 1.5 inch (off focal point) from the lamp as shown in Figure 2.2. The optical fluence at the substrate was obtained via the inverse square law by using the known E_p based on the on-time and voltage used, and the known distance of the substrate from the

focal point of the lamp. This method for calculation of the optical power was further confirmed by experimental measurement of optical power using a Gamma Scientific S471 optometer that had a nearly 95% relative response within a 400-700 nm wavelength range. Table 2.1 shows the IPL parameters used in this work and the calculated energy density at the substrate.

Table 2.1 IPL Parameters for 20 nm and 40 nm silver nanoparticles

Voltage (kV)	On time/ Off time (milliseconds)	Fluence per pulse at substrate (J/cm²)	No. of pulses
2.2	0.250/ 121	E1=0.85	50, 90,150
2.5	0.260/ 143	E2=1.2	
2.8	0.255/ 160	E3=1.6	

2.1.3 Film characterization:

A thermal camera (MicroEpsilon thermoimager TIM 200, maximum temperature 1500°C, error $\pm 2\%$) was used to measure the temperature of the Ag film during IPL. The emissivity of the Ag films was manually calibrated within the IPL setup by heating the coated film and glass slab to 130 °C on a hot plate, till the Ag film reached a steady state temperature. The evolution of film emissivity during IPL was measured by performing IPL on distinct spin-coated samples, for different number of pulses at fluence values shown in table 2.1, and calibrating the emissivity after IPL for each sample as described above (Figure 2.3). The emissivity was captured as a function of the number of pulses at each

fluence via non-linear least square interpolation. The emissivity compensated temperature evolution during IPL was obtained based on the Stefan-Boltzmann law.

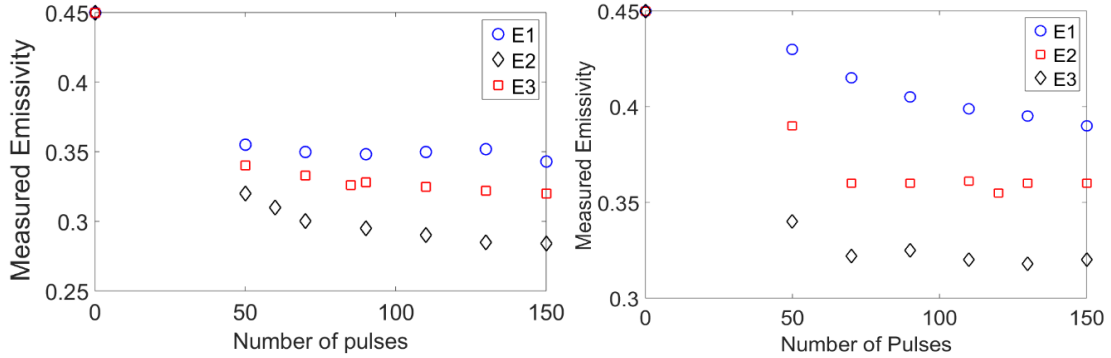


Figure 2.3. Measured emissivity as a function of number of IPL pulses and pulse fluence for (a) 20 nm and (b) 40 nm Ag nanoparticle films

The change in particle size during IPL was characterized as a function of fluence and number of pulses, via processing of Scanning Electron Microscopy images of sintered and unsintered films using ImageJ open source software. θ - 2θ X-ray Diffraction (Bruker AXS D8 Discover) and measurement of film resistance via a Signatone four-point probe, were used to additionally quantify sintering during IPL as a function of fluence and number of pulses.

2.2 Computational Modeling

The computational model developed for predicting temperature and density evolution in IPL consists of a nanoscale model, and a mesoscale model that is informed by the nanoscale model. The nanoscale model is described first, followed by a description of the mesoscale model and the manner in which these two models are linked.

2.2.1 Nanoscale Model:

The nanoscale model explicitly couples optical absorption in an ensemble of Ag nanoparticles to equilibrium geometric configurations of the nanoparticle ensemble due to interparticle neck growth. The goal is to quantify the evolution of optical absorption induced heating as a function of interparticle neck growth, and the corresponding change in volume fraction, due to sintering during IPL. Electromagnetic field simulations were performed using COMSOL FEA for an idealized non-randomly packed ensemble of five spherical Ag nanoparticles with an incident electric field of magnitude 1 V/m travelling along direction \mathbf{k} and linearly polarized along direction \mathbf{E} (figure 2.4). The nanoparticles were placed inside a spherical air shell, which was surrounded by a perfectly matched layer to prevent spurious reflections. The wavelength dependent real and imaginary dielectric constants of Ag were obtained via the Drude-Lorentz model[54]. The mesh size, size of air shell and size of the perfectly matched layer were refined till their effect on the predicted absorption and scattering curves was negligible.

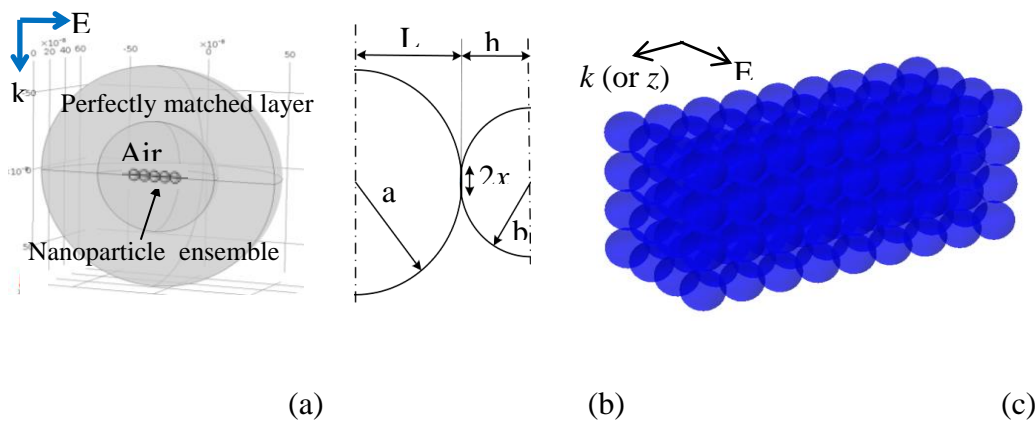


Figure 2.4: Schematic of (a) COMSOL FEA for an ensemble of five Ag nanoparticles (b) two unequal size nanoparticles with the relevant geometrical parameters used in the nanoscale sintering model (c) Ag nanoparticle layers used in COMSOL FEA.

To calculate optically induced heating in such a nanoparticle ensemble as a function of interparticle necking via the above FEA, it is necessary to first calculate intermediate equilibrium configurations of the nanoparticle ensemble during sintering. Note that these intermediate configurations should not violate conservation laws. Neck growth between adjacent nanoparticles in the ensemble was captured in terms of the geometric parameters at each interparticle contact (figure 2.4b, shown for a case of two unequally sized nanoparticles). The evolution of the geometric parameters was governed by equilibrium geometric configurations of the ensemble, obtained by modifying a McMeeking-Cocks-Suo model[55] to account for the absence of externally applied pressure during IPL. The evolution of a and b in this sintering model is described using a matrix k and the generalized driving vector components f_1 and f_2 in (1)-(4). In (2) the terms g_a and g_b are simply shorter expressions involving the geometric parameters shown in Figure 2.4b, and are expressed as $g_a = \ln[a/x(a + \sqrt{1 - x^2/a^2})] - L/a$ and $g_b = \ln[b/x(b + \sqrt{1 - x^2/b^2})] - h/b$. As shown in (2)-(5), the k , f_1 and f_2 depend on the thickness of the region with enhanced grain boundary and surface diffusion (δ_b and δ_s , respectively), grain boundary and surface atom diffusivities (D_b and D_s , respectively), grain boundary and surface energies per unit area (γ_b and γ_s , respectively), atomic volume Ω , Boltzmann constant k , and temperature T in Kelvin.

$$[k] \begin{bmatrix} a \\ b \end{bmatrix} = \begin{bmatrix} f_1 \\ f_2 \end{bmatrix} \quad (1)$$

$$k = \begin{bmatrix} \frac{2\pi a^4 g_a kT}{\delta_s D_s \Omega} + \frac{\pi a^2 L^2 kT}{2\delta_b D_b \Omega} & \frac{\pi abLhkT}{2\delta_b D_b \Omega} \\ \frac{\pi abLhkT}{2\delta_b D_b \Omega} & \frac{2\pi b^4 g_b kT}{\delta_s D_s \Omega} + \frac{\pi b^2 h^2 kT}{2\delta_b D_b \Omega} \end{bmatrix} \quad (2)$$

$$f_1 = -2\pi\gamma_b \frac{ah(a^2 + L^2)}{x^2(h+L)} - 2\pi\gamma_s L - \frac{2\pi\gamma_s a}{x^2(h+L)} \{a(x^2 - 2hL) - b(a^2 + L^2)\}$$

(3)

$$f_2 = -2\pi\gamma_b \frac{bL(b^2 + h^2)}{x^2(h+L)} - 2\pi\gamma_s h - \frac{2\pi\gamma_s b}{x^2(h+L)} \{b(x^2 - 2hL) - a(b^2 + h^2)\} \quad (4)$$

Equations (1)-(4) can be used with the conservation of mass (as in (5), where a_0 and b_0 are the initial diameters of larger and smaller nanoparticles respectively) and the retention of geometric constraints between two nanoparticles in (6), to track the evolution of neck growth between adjacent nanoparticles as a function of the temperature T .

$$\left(a^2 L - \frac{L^3}{3}\right) + \left(b^2 h - \frac{h^3}{3}\right) = \left(\frac{4}{3}\right)(a_0^3 + b_0^3) \quad (5)$$

$$L^2 = a^2 - x^2, h^2 = b^2 - x^2 \quad (6)$$

In this work, we assumed that grain boundary diffusion and surface diffusion have equal contributions to mass transfer during neck growth, i.e., $\delta_b = \delta_s$, and $D_b = D_s = D_0 e^{-E/kT}$, where E is the activation energy and D_0 is a pre-exponential factor. Further, uniformly sized nanoparticles were modeled, i.e., $a = b$ and $L = h$. This analytical neck growth model was implemented using the material parameters shown in table 2.2 and a prescribed temperature ramp of 400 K/min over 1 minute. At each time step during the temperature ramp, forward Euler integration was used to update a and b using (1)-(4), followed by calculation of L , h and x using (5) and (6). The evolving equilibrium configurations of the nanoparticle ensemble during sintering, with each configuration abiding by conservation laws, were thus obtained. Note that the values of the material parameters and the temperature ramp

rate used in this model were only used to obtain equilibrium geometric configurations for the ensemble, and not to directly calculate the mesoscale densification of the Ag film.

Table 2.2. Model parameters used

Parameter	Value
γ_b	7.12 J/m^2 [56]
γ_s	1.31 J/m^2 [56]
$\delta_b (= \delta_s)$	0.5 nm [57]
Ω	$10.27 \text{ cm}^3/\text{mol}$ [58]
D_0	$0.724 \text{ m}^2/\text{s}$ [57]
E	$45,500 \text{ J/mol}$ [57]

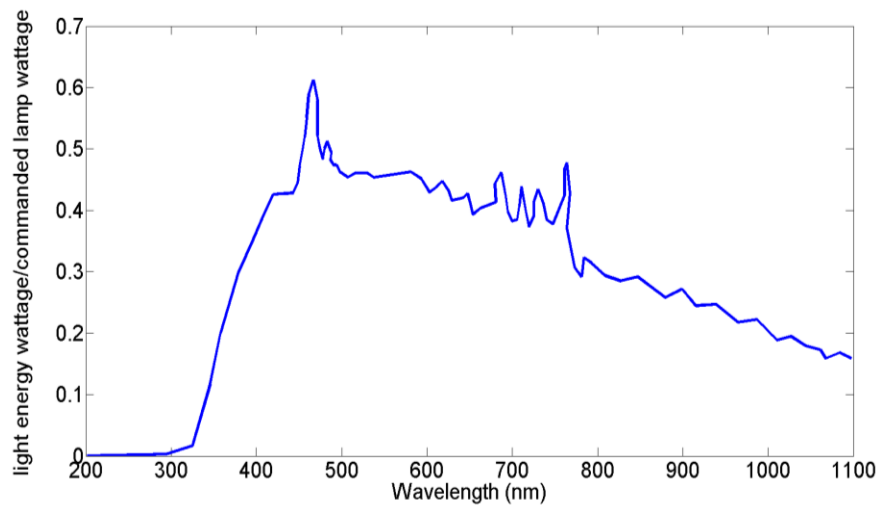
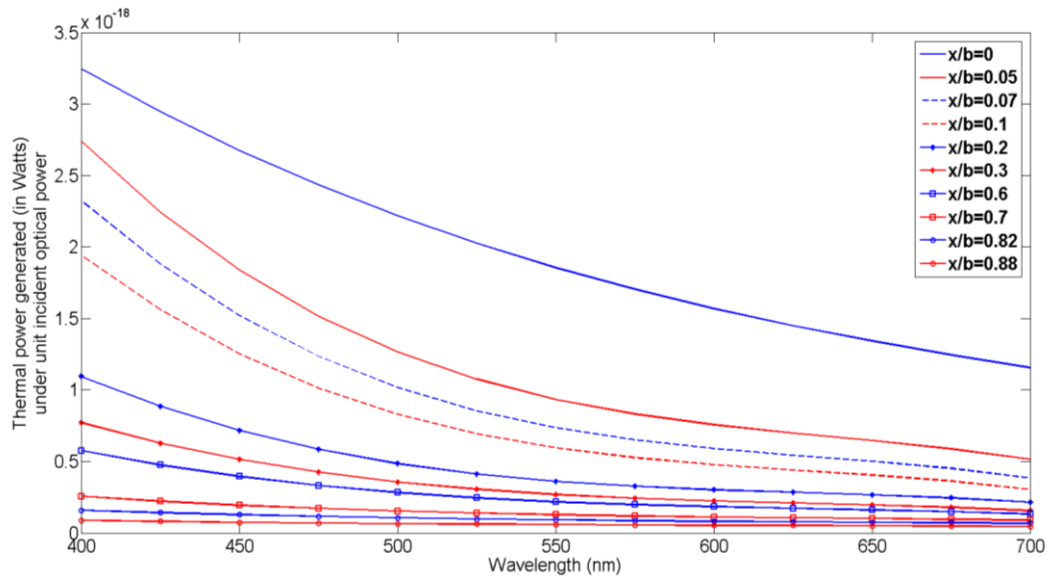
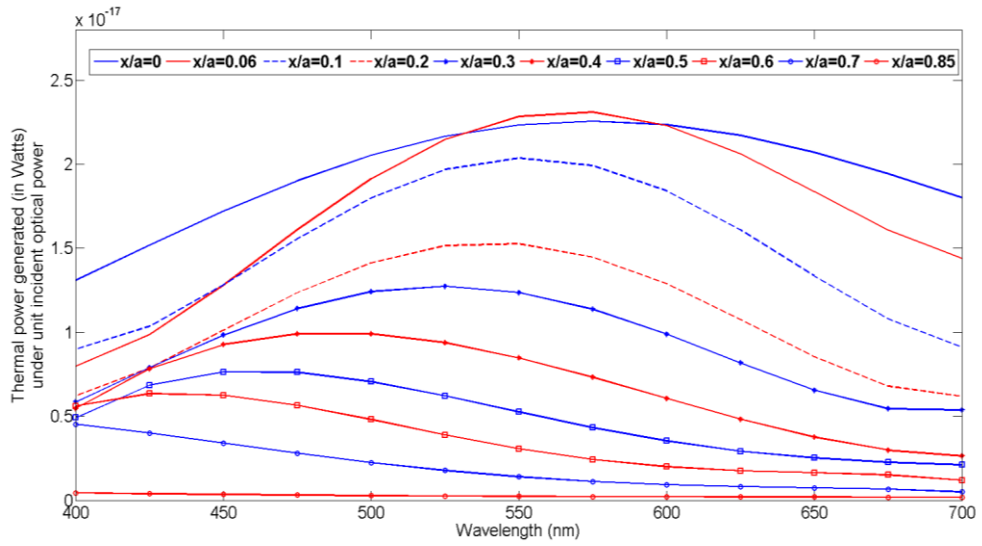


Figure 2.5: Spectral output of the Sinteron 3000 IPL system

For each equilibrium configuration of the nanoparticle ensemble, distinct electromagnetic FEA were performed over optical wavelengths λ from 400 nm to 700 nm, within which most of the energy from the xenon lamp lies (Figure 2.5). The total thermal power dissipation as a function of λ , i.e., Q_λ , for distinct ensemble configurations was calculated by integrating the thermal power dissipation density over the ensemble volume within COMSOL (see Figure 2.6). A blue shift and a reduction in magnitude of peak absorption intensity in the visible spectrum was observed with an increase in interparticle neck size, as has also been observed in past literature [59,60]. The total heat generated per unit apparent volume in the ensemble, i.e., Q_s , was obtained by integrating the product of Q_λ with the normalized optical energy from the lamp at a given wavelength over $\lambda = 400$ nm to 700 nm, and dividing the integral by the original bounding volume of the ensemble. The volume fraction θ corresponding to each sintered configuration was obtained from the bounding volume of the configuration and by calculating the actual solid volume of the nanoparticle ensemble as a function of the geometric parameters. The function $Q_s(\theta)$ was thus calculated. To model optically induced heating as a function of the depth in the nanoparticle film, the unsintered nanoparticle ensemble was extended to 10 nanoparticles in the direction of the film thickness, i.e., along the direction of travel of the light (k or z direction in Figure 2.4c). Electromagnetic FEA for this unsintered nanoparticle ensemble were performed over wavelengths 400 nm to 700 nm, to calculate Q_s in each nanoparticle layer as above. The ratio of Q_s in each layer to that in the topmost layer of the nanoparticles, i.e., the normalized function $Q_s(z)$ where z is the coordinate of the center of a nanoparticle in the direction of the film thickness, was thus obtained.



(a)



(b)

Figure 2.6: Predicted thermal power per unit incident optical power, i.e., Q_{λ} , for Ag nanoparticle ensembles shown in figure 2.4 a with nanoparticle diameters (a) 20 nm (b) 40 nm.

2.2.2 Mesoscale Model:

The functions $Q_s(\theta)$ and $Q_s(z)$ were used in a model that coupled mesoscale heat transfer and densification in the Ag film during IPL. This mesoscale model (Figure 2.7) consisted of a $10\ \mu\text{m}$ thick layer of silver over a $25\ \text{mm} \times 25\ \text{mm}$ area on a $250\ \mu\text{m}$ thick Kapton film, which in turn was kept on a $2.5\ \text{mm}$ thick glass plate that could conduct heat to the surroundings, as in experiments. The following assumptions were made. Conductive heat transfer occurs primarily in the thickness direction, since the maximum temperature gradient is in that direction. Convective losses occur only via the top surface of the film, since the film fully covers the substrate and the area of the side walls of the assembly is much smaller than that of the top surface of the film. These assumptions essentially reduced the heat transfer problem to one-dimension (i.e., along direction z in Figure 2.7).

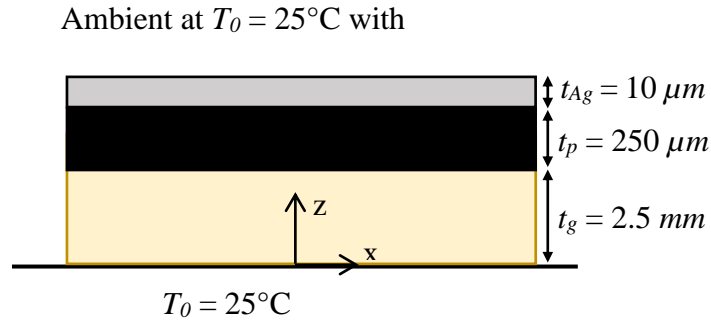


Figure 2.7: Schematic of the mesoscale model (dimensions not to scale).

The high thermal conductivity of Ag even in porous film form, the small characteristic length of the Ag film and the low thermal conductivity of the Kapton film as compared to the silver film results in the Biot number for the silver film being much smaller than 1. Thus, the silver film was assumed to be at a uniform temperature at any point of

time. Interfacial thermal resistance between the Ag film, Kapton and glass was assumed to be negligible. The bottom surface of the glass was always at ambient temperature, i.e., $T_0 = 25^\circ\text{C}$. Expansion and shrinkage induced changes in dimension of the Ag film and of the Kapton substrate were neglected. Further, it was assumed that the nanoparticle packing in the mesoscale Ag film is identical to that shown in Figure 2.4c. The temperature evolution in the assembly at any time τ during IPL, was calculated by simultaneously solving the lumped capacitance model for the silver film in (7) and the explicit finite-difference form of the heat transfer equation for the Kapton and glass in (8). The system was subject to boundary conditions shown in (9).

$$\frac{\partial Q_{Ag}}{\partial \tau} = (\rho C)_{eff} \frac{\partial T_{Ag}(\tau)}{\partial \tau} + \frac{h(T_{Ag}(\tau) - T_0)}{t_{Ag}} + Q_{cond}(\tau) \quad (7)$$

$$\frac{\partial}{\partial z} \left(K_{p/g} \frac{\partial T_{p/g}(\tau)}{\partial z} \right) = \rho_{p/g} C_{p/g} \frac{\partial T_{p/g}(\tau)}{\partial \tau} \quad (8)$$

$$T_p(\tau) = T_{Ag} \text{ at } z = t_p + t_g \text{ and } T_{glass}(\tau) = T_0 \text{ at } z = 0 \quad (9)$$

In (7) - (9) the subscript *Ag* denotes the property or temperature for Ag film, subscript *p/g* denotes the property or temperature for polymer or glass respectively depending on whether (8) is being solved for the kapton or for the glass, subscript *0* denotes ambient and initial condition, and *T* denotes temperature. Further, *h* is the convective heat transfer coefficient, ρ denotes density and *C* denotes specific heat capacity. The effective volumetric heat capacity of the silver film $(\rho C)_{eff}$ was modeled as $(\rho C)_{eff} = \rho_{Ag} C_{Ag} \theta + \rho_{Air} C_{Air} (1 - \theta)$ after Nield et al. [61], where the subscript *Air* denotes the properties of air as the medium in the pores in the Ag film and θ is the solid volume fraction

of Ag in the film. The optically induced internal thermal power per unit volume of the Ag film, i.e., Q_{Ag} in (7) is

$$Q_{Ag} = g [0,1] \sqrt{120\pi P} \left(\int_0^{t_{Ag}} Q_s(\theta) Q_s(z) dz \right) \quad (10)$$

where the functions $Q_s(\theta)$ and $Q_s(z)$ were obtained from the nanoscale model for a given nominal nanoparticle diameter and a unit incident electric field, the function g is a binary function equaling 1 when the light pulse is on and 0 when the light pulse is off, P is the peak incident irradiance of the xenon lamp light so that $(120\pi P)^{1/2}$ yields the incident electric field intensity in V/m based on the characteristic impedance of free space. In (7), Q_{cond} is the volumetric thermal power lost by the Ag film via conduction to the polymer-glass assembly at any time τ .

The evolution of θ with T_{Ag} was modeled using a linear Master Sintering Curve (MSC) [62] in (11), where E_{act} is the activation energy for sintering and is specific to the nanoparticle size, nanoparticle material and film preparation method, and R is the universal gas constant. The constants C_1 and C_2 represent the shape of the MSC.

$$\theta(\tau, T_{Ag}(\tau)) = C_1 \log_{10} \left\{ \int_0^\tau \frac{1}{T_{Ag}} \exp \left(\frac{-E_{act}}{R(T_{Ag} - T_0)} \right) d\tau \right\} + C_2 \quad (11)$$

The calibration of even this simple MSC requires dilatometry data which is hard to obtain for thin films. The form of $Q_s(\theta)$ obtained from nanoscale modeling (shown later in section 3.2) allows the parameters E_{act} , C_1 and C_2 in (11) to be calibrated by matching predicted evolution of film temperature from the mesoscale model to that measured in

experiments. For example, the parameter E_{act} primarily influences the temperature turning point, with greater E_{act} resulting in a higher temperature turning point (e.g., see Figure 2.8).

Table 2.3. Thermal properties and calibrated MSC parameters used for mesoscale modeling.

Property	Ag	Kapton	Glass
Thermal Conductivity (W/m-K)	400	0.12	0.8
Specific Heat Capacity (J/Kg-K)	235	1090	840
Density of material (Kg/m³)	10490	1420	2500
Convective heat transfer coefficient h (W/m²-K)	20		
Calibrated activation energy E_{act} (kJ/mol)	20 nm Ag: 117.5; 40 nm Ag: 142.5		
Calibrated C_1	20 nm Ag: 0.01; 40 nm Ag: 0.01		
Calibrated C_2	20 nm Ag: 1.01; 40 nm Ag: 0.90		

The parameter C_1 influences the slope of the temperature curve after the temperature turning point. Greater C_1 results in faster drop in temperature after the temperature turning point, and vice versa. For any trial E_{act} and C_1 , the value of C_2 was calculated based on the assumption that the initial θ was 0.71, as calculated from the idealized packing configuration on which the nanoscale model (Figure 2.4c) was based. In this work the parameters E_{act} , C_1 and C_2 were calibrated for both 20 nm and 40 nm

nanoparticle films via multiple trial and error runs of the model for fluence E_2 , and comparison of predicted film temperature evolution to the experimentally measured film temperature evolution. The mesoscale simulations were stopped when the total number of specified pulses were reached. Further, $\theta \leq 0.95$ was enforced. The values of the thermal properties used in this mesoscale model, as well as the calibrated values of E_{act} , C_1 and C_2 for both nanoparticle sizes, are shown in table 2.3

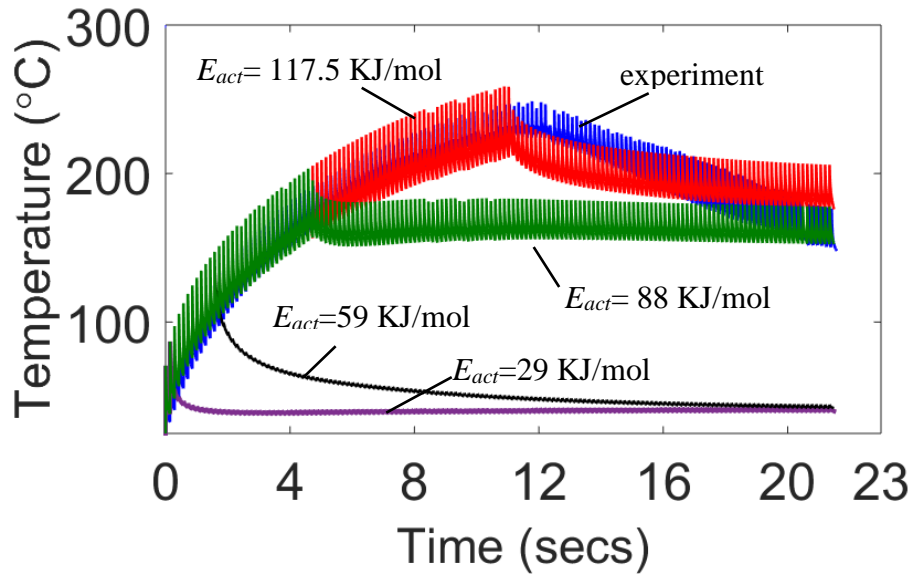


Figure 2.8: Effect of activation energy E_{act} on predicted temperature evolution as compared to experimental evolution of temperature for fluence E_2 on 20 nm Ag nanoparticle film.

The evolution of θ as a function of the temperature history of the film is represented by the MSC in (11). The θ in turn is capable of affecting heat transfer and therefore the temperature rise in the film via its inclusion in (10) as $Q_s(\theta)$ and in (7) as Q_{Ag} , as well as its effect on the $(\rho C)_{eff}$ of the film. Further, $Q_s(\theta)$ and $Q_s(z)$ are the key terms via which the nanoscale model informs the above mesoscale model. Note that the form taken by the function $Q_s(\theta)$ is not subject to any arbitrary constraints imposed by the authors. Since the

$Q_s(\theta)$ is obtained from the full field electromagnetic FEA in the nanoscale model, the volume fraction θ is able to affect temperature evolution in a physically realistic manner. Thus, equations (7) to (11) couple the dependence of optical heating on nanoscale densification to the mesoscale temperature rise and densification, albeit explicitly. In addition to the above coupled model, an uncoupled mesoscale model was also used to predict temperature rise and densification in the Ag film. This uncoupled model was based on the conventional assumption that optical heating is independent of the volume fraction of Ag in the film, i.e., interparticle necking during IPL does not affect optical absorption significantly. This was implemented by forcing the condition $Q_s(\theta) = Q_s(0.71)$ in (10) at any point of time in the mesoscale model. This forced the Q_{Ag} in (7) to be constant for every IPL pulse, and to correspond to the initial optical absorption by the unsintered film.

3 Results and Discussion

3.1 Experimental Results

3.1.1 Temperature evolution

Figure 3.1 shows the measured evolution of film temperature over 150 IPL pulses at different fluences, along with the specific time points corresponding to 50, 90 and 150 pulses. The following observations can be made. As expected, the increase in film temperature per pulse is greater for higher fluence ($E3 > E2 > E1$) for both 20 nm and 40 nm nanoparticle films. For both nanoparticle sizes there is a monotonic increase in temperature at fluence E1. However, for fluence E2 and E3 there is a turning point in temperature (marked in Figure 3.1) after which the temperature starts to reduce despite no change in the commanded fluence. For the same fluence and number of pulses, the 40 nm nanoparticle film sees a greater rise in temperature per pulse than the 20 nm nanoparticle film. This can be attributed to greater volumetric heating per unit incident optical energy by larger nanoparticles [63]. Furthermore, there is a slight increase of turning point temperature from fluence E2 to fluence E3. This increase in temperature is no more than 5°C , which is within the 2% error of the thermal camera used in this work. Thus, this is likely not a real physical effect but an artifact of the relatively small error in temperature measurement. For all the cases shown in Figure 3.1 the film temperature does not exceed the melting point temperature (approximately 927°C) or the surface pre-melting temperature of the corresponding nanoparticles (approximately 727°C) even after accounting for nanoparticle size effects[64]. This indicates that melting of nanoparticles in

the film is unlikely during these IPL experiments, which is why melting and the accompanying latent heat of fusion is not considered in the developed model.

* E1-50 pulses ○ E1-90 pulses □ E1-150 pulses * E2-50 pulses ○ E2-90 pulses □ E2-150 pulses
 * E3-50 pulses ○ E3-90 pulses □ E3-150 pulses

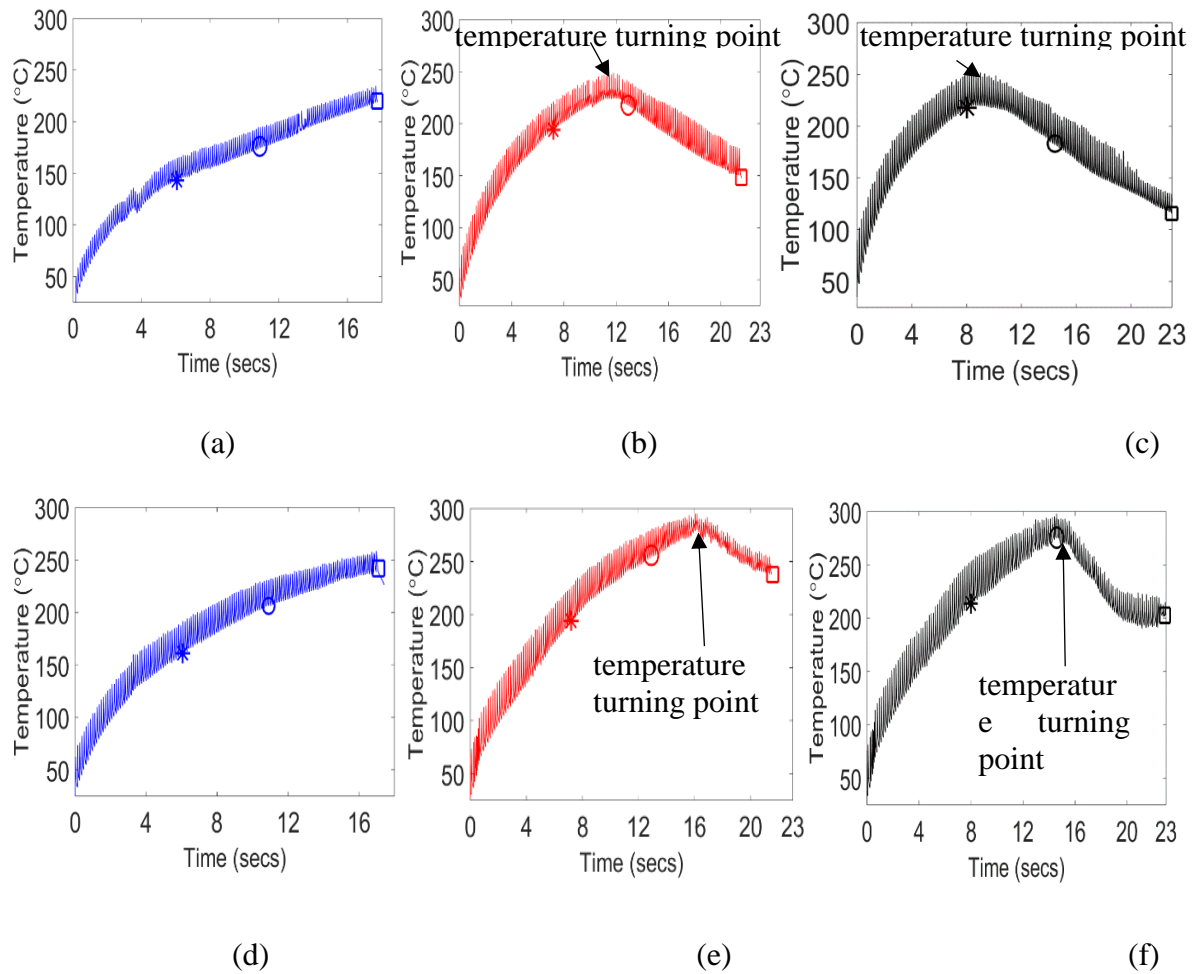
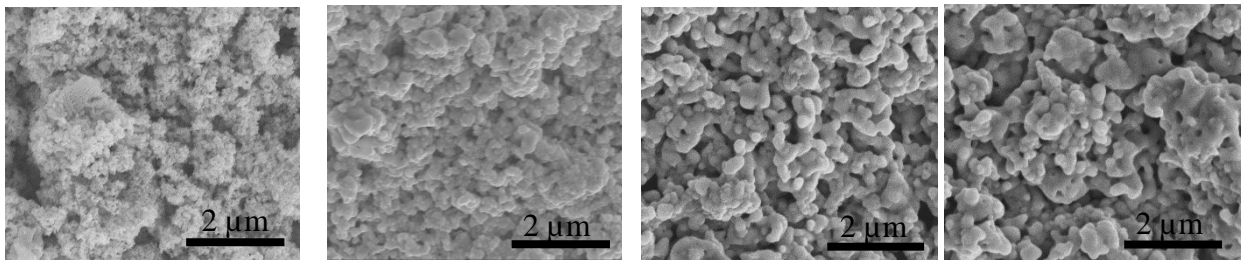


Figure 3.1: Temperature evolution over 150 pulses during IPL of 20 nm diameter nanoparticle films at fluence (a) E1 (b) E2 (c) E3; and during IPL of 40 nm films at fluence (d) E1 (e) E2 (f) E3.

3.1.2 Morphological change

SEM images of the unsintered and sintered films (Figure 3.2 a-d and Figure 3.3a-d, and Figure 3.4 and Figure 3.5) show interparticle neck growth and increase in particle size in the film after IPL. Further, cross-sectional SEM of the sintered nanoparticles near the substrate (Figure 3.2e-g; Figure 3.3e-g) shows no significant change in interparticle necking through the thickness of the film. Since densification in IPL is only a function of the temperature, this observation also indicates a nearly uniform temperature through the thickness of the deposited films during IPL. While no burning of the film or the substrate was seen in these experiments, cracking of the film was observed, as shown in figures 3.2h-k for the 20 nm film. At the same number of pulses, the size of cracks increased with greater fluence, which has also been observed in literature [2, 24] and is likely due to densification induced stresses. At a constant fluence the crack size and number seemed to increase with increasing number of pulses, which is again likely due to densification induced stresses.

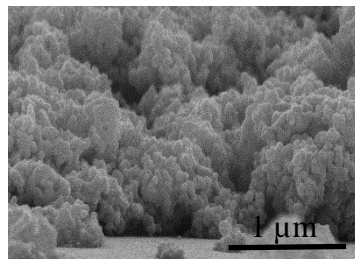


(a)

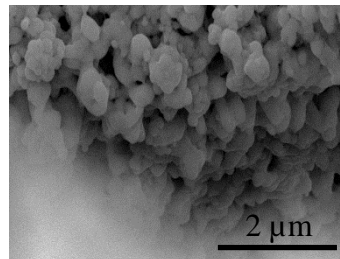
(b)

(c)

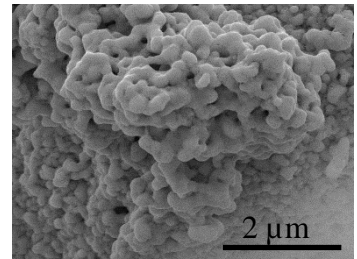
(d)



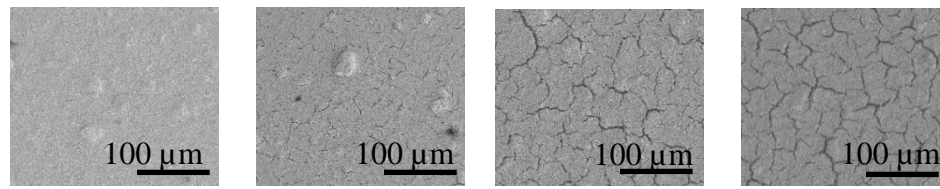
(e)



(f)



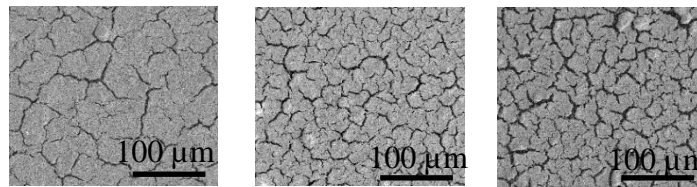
(g)



Increasing number of pulses →

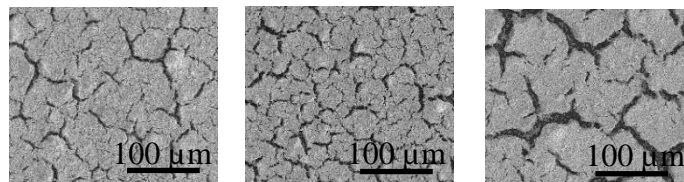
(h) Unsintered film

(i) Fluence E1



Increasing number of pulses →

(j) Fluence E2



Increasing number of pulses →

(k) Fluence E3

Figure 3.2: Planar SEM micrographs of 20 nm Ag film (a) unsintered; and sintered with 150 IPL pulses at fluence (b) E1 (c) E2 (d) E3. Cross-sectional SEM images of 20 nm Ag film near substrate for 150 IPL pulses at fluence (e) E1 (f) E2 (g) E3. Larger scale planar SEM micrographs for 20 nm Ag film (h) unsintered (i) sintered at fluence E1 (j) sintered at fluence E2 (k) sintered at fluence E3.

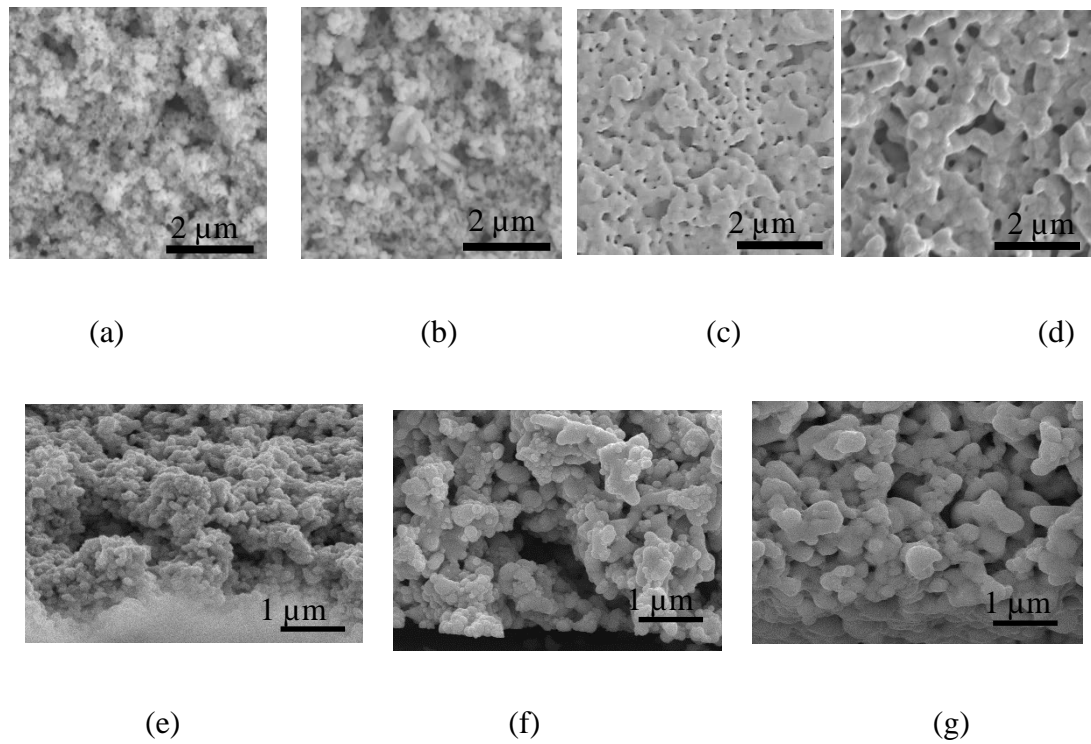


Figure 3.3: SEM micrographs of 40 nm Ag film (a) unsintered; and sintered with 150 IPL pulses at fluence (b) E1 (c) E2 (d) E3. Cross-sectional SEM images of 40 nm Ag film near substrate for 150 IPL pulses at fluence (e) E1 (f) E2 (g) E3.

However, a key observation is that cracking increased even beyond the temperature turning point. It is relevant to note that, as shown later, the change in the sheet resistance and in nanoparticle densification beyond the temperature turning point is not significant. This indicates that increased cracking beyond the temperature turning point might be more due to thermal shock induced expansion and contraction of the material rather than due to stresses induced by densification. Similar trends were also observed in the case of 40 nm films (Figure 3.5).

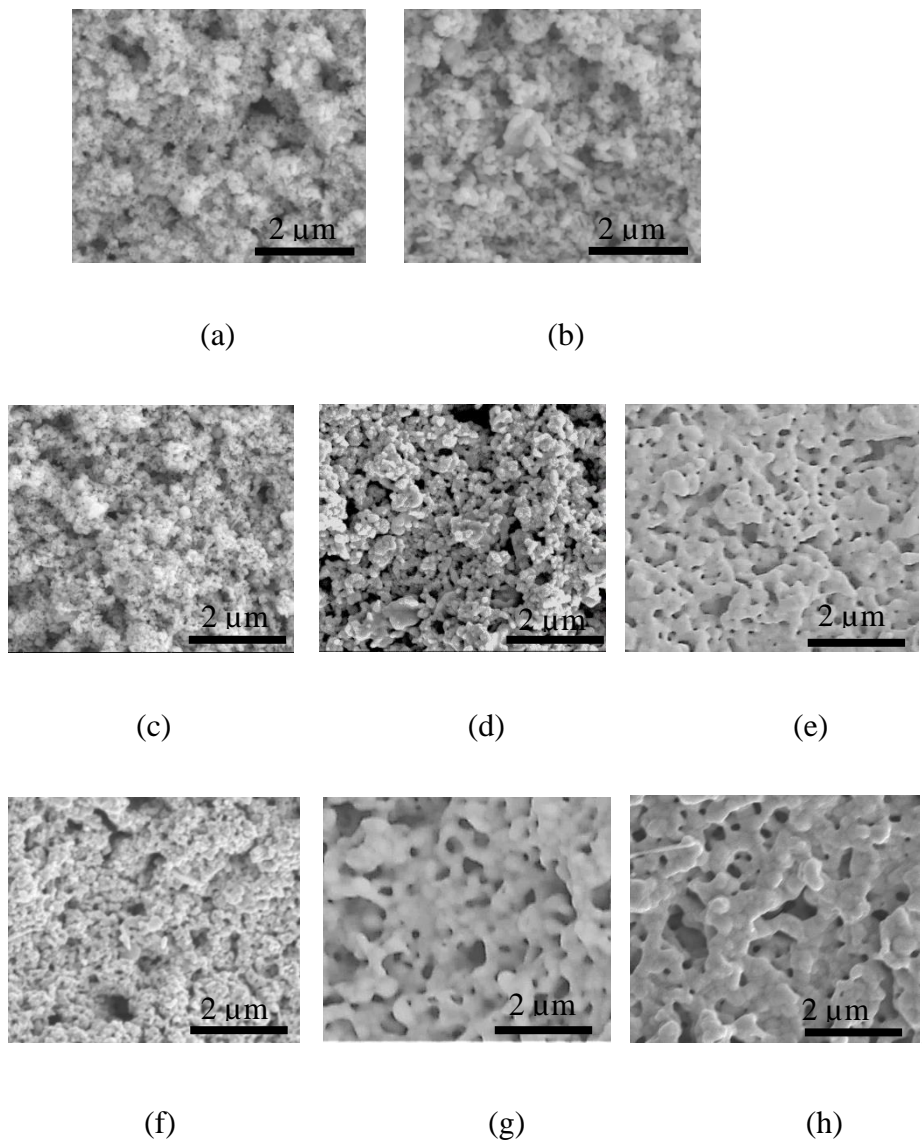
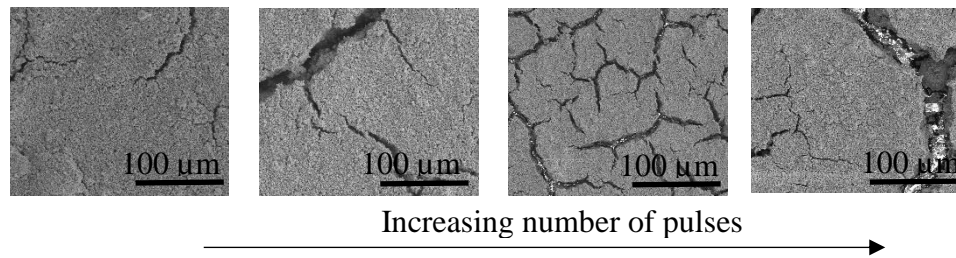
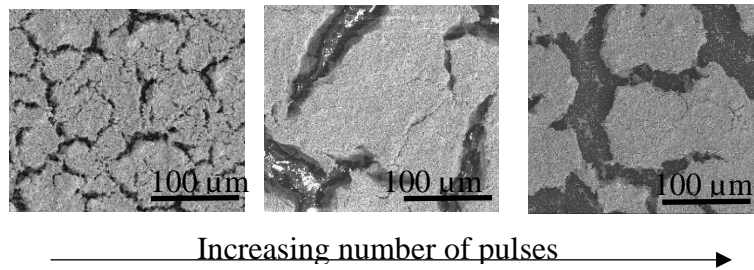


Figure 3.4: SEM micrographs of 40 nm Ag nanoparticle films (a) unsintered; and IPL sintered with (b) E1-150 pulses (c) E2-50 pulses (d) E2-90 pulses (e) E2-150 pulses (f) E3-50 pulses (g) E3-90 pulses (h) E3-150 pulses.

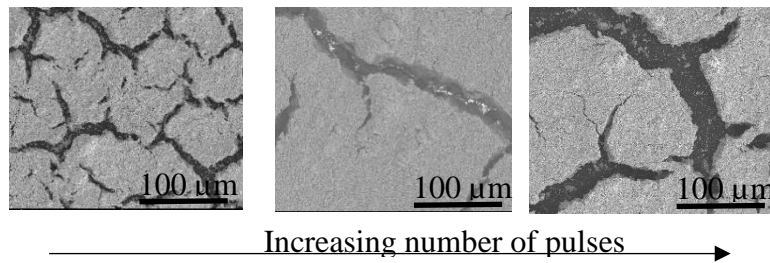


(a) Unsintered film

(b) Fluence E1



(c) Fluence E2



(d) Fluence E3

Figure 3.5: Larger scale planar SEM micrographs for 40 nm Ag film (a) unsintered (b) sintered at fluence E1 (c) sintered at fluence E2 (d) sintered at fluence E3.

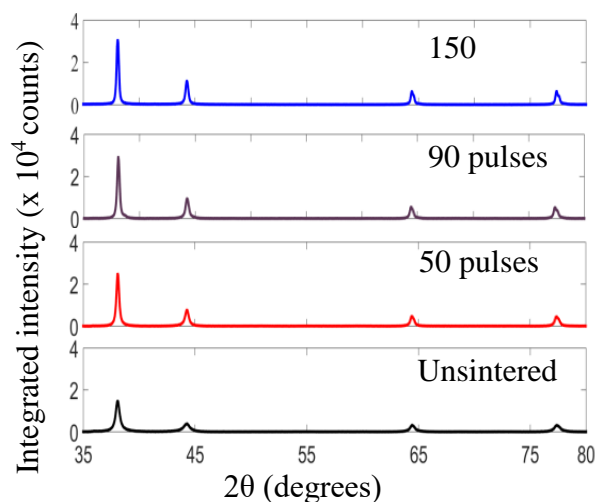
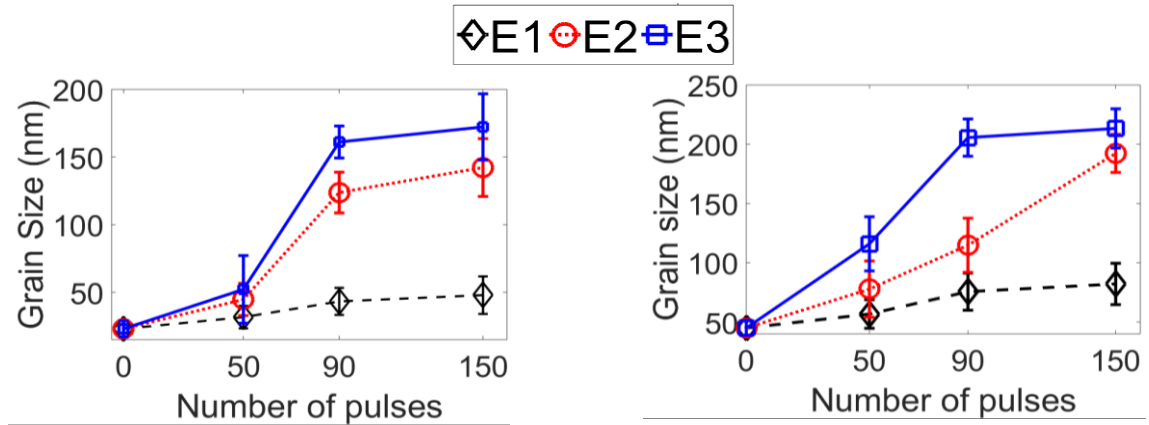


Figure 3.6: Representative XRD curves for unsintered and sintered 20 nm Ag nanoparticle film, as a function of number of pulses, for fluence E3.

3.1.3 Particle size and Sheet Resistance

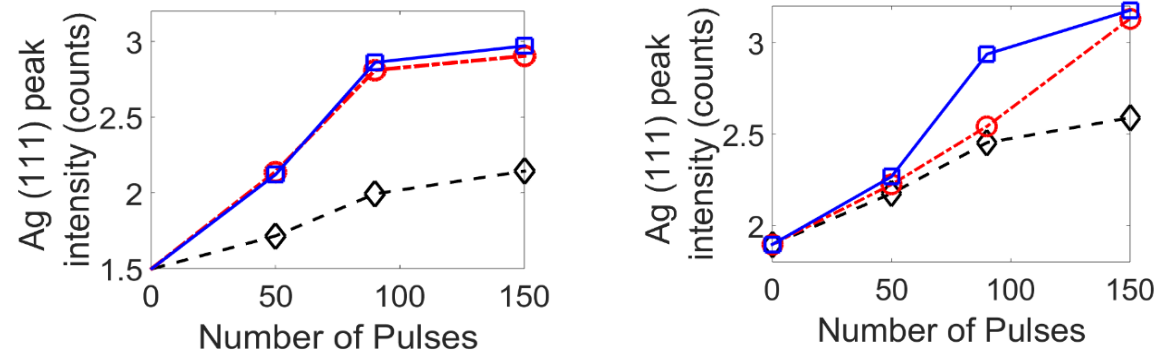
X-ray diffraction (Figure 3.6 shows representative intensity versus 2θ curves) shows a general increase in peak intensity and reduction in Full Width at Half Maximum (FWHM) after IPL. This indicates a reduction in the available free surface and increase in crystallinity and stresses due to interparticle neck growth [65]. Overall, the evolution of particle size (Figure 3.7a-b), and of the peak intensity (Figure 3.7c-d) and FWHM (Figure 3.7e-f) for the dominant Ag (111) peak, shows greater sintering with greater fluence which is as expected from past work on IPL [6, 24]. For 20 nm films (Figure 3.7a, c, e) a significant increase in densification can be observed at 90 pulses for fluence E2 and E3, which lies beyond the temperature turning point (Figure 3.1b and Figure 3.1c). However, beyond 90 pulses the rate of increase in sintering slows down as indicated by the grain sizes, peak intensity and FWHM beyond 90 pulses. This reduction in densification after

the temperature turning point is also reflected in the sheet resistance (Figure 3.7g), which reduces to around 0.15 ohms/sq. at 90 pulses for fluence E1 and E2 but levels off after 90 pulses, as compared to nearly no reduction in resistance for fluence E1.



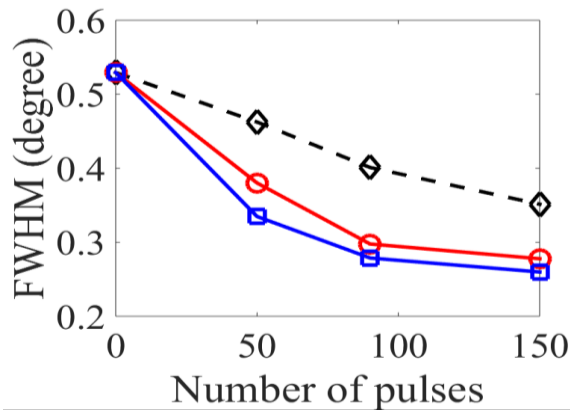
(a)

(b)

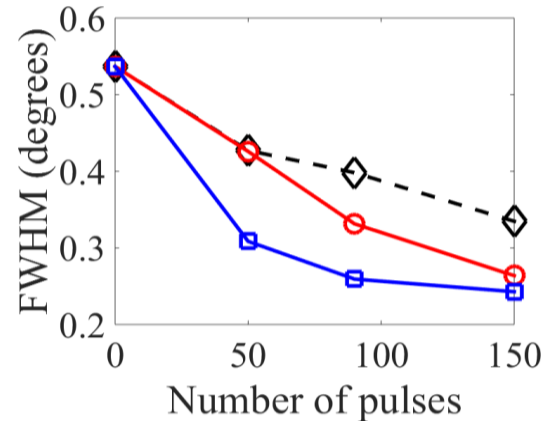


(c)

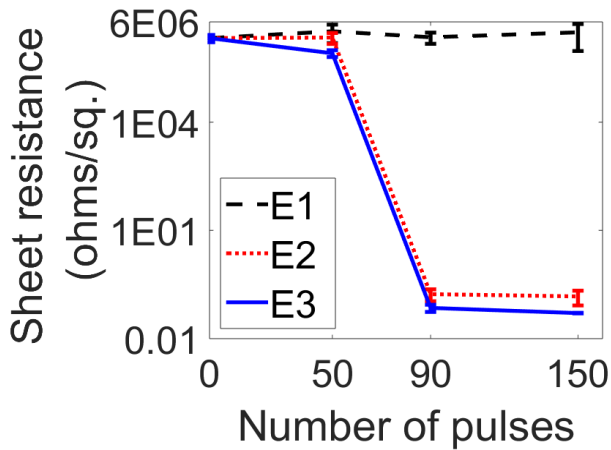
(d)



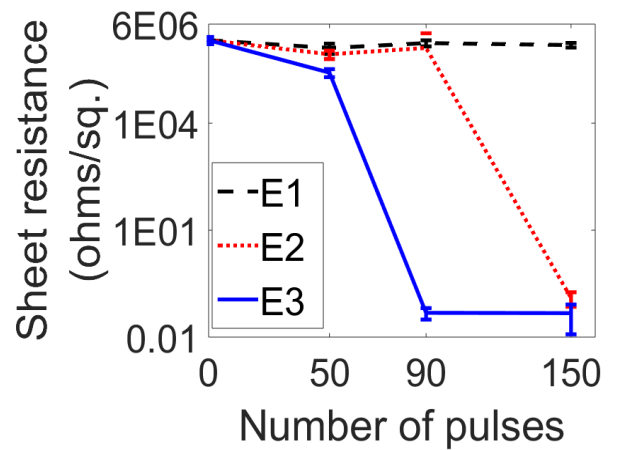
(e)



(f)



(g)



(h)

Figure 3.7: Change in particle size with number of pulses and fluence for (a) 20 nm Ag film (b) 40 nm Ag film. Error bars show standard deviation in measured particle size. Change in Ag (111) peak intensity with number of pulses and fluence for (c) 20 nm Ag film (d) 40 nm Ag film. Change in FWHM at Ag (111) peak with number of pulses and fluence for (e) 20 nm Ag film (f) 40 nm Ag film. Change in sheet resistance with number of pulses and fluence for (g) 20 nm Ag film (g) 40 nm Ag film.

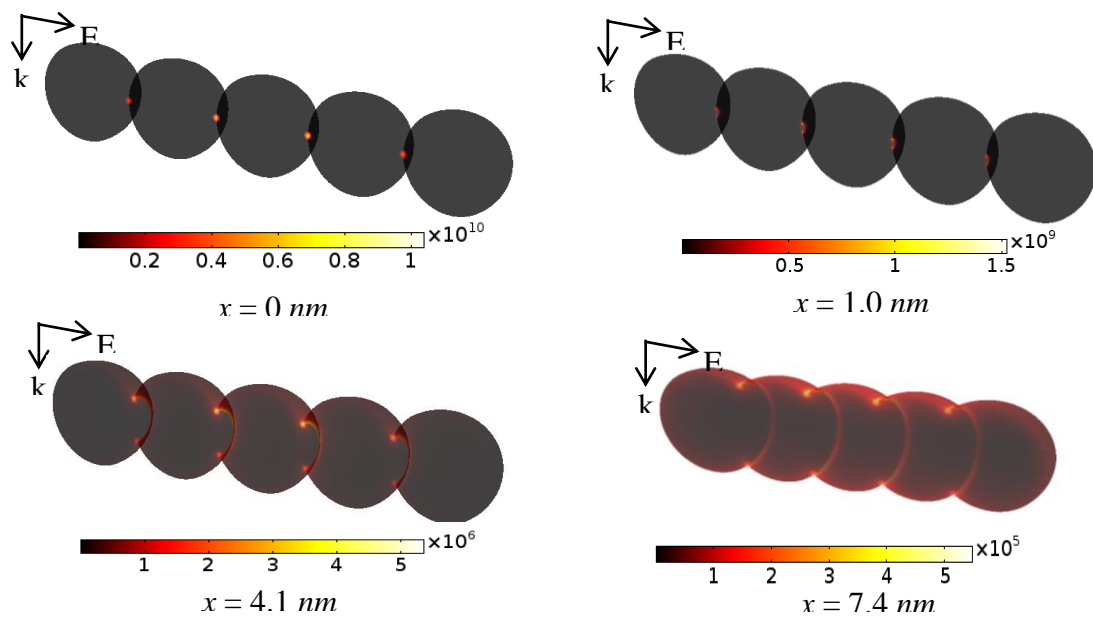
For 40 nm nanoparticle films at fluence E2, 90 pulses does not lie beyond the temperature turning point (Figure 3.1e) and so an increase in sintering can only be seen at 150 pulses (Figure 3.7b, d, f). For fluence E3, 90 pulses is very close to the temperature

turning point (Figure 3.1f) and an increase in sintering is seen (Figure 3.7b, d, f). After this point, again the rate of densification seems to reduce. This observation is also reflected in the reduction in sheet resistance near the turning point temperature and little change after (Figure 3.7h).

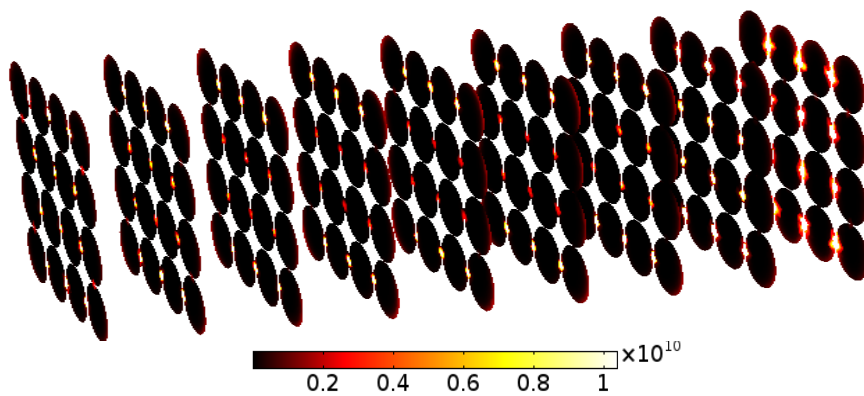
Overall, these trends indicate an increase in rate of densification near the temperature turning point, and a subsequent reduction after it. Since no external pressure is applied during IPL, and the nanoparticle size, deposition method, and nanoparticle material are kept the same, the film temperature is the primary factor that governs densification in these IPL experiments. Therefore, the reduction in rate of densification beyond a critical number of pulses corresponding to the turning point temperature is due to a reduction in the film temperature beyond this critical number of pulses. The next section presents predictions from the models developed in section 2.2.2 to answer the question, why does the turning point in temperature occur in the first place?

3.2 Predictions from Modeling

Figure 3.8a shows representative contours of volumetric thermal power dissipation in the five nanoparticle ensemble as a function of different neck radii x , as predicted by electromagnetic FEA in Figure 2.4a. Note that the volumetric power dissipation is highest at the interface between the two nanoparticles, before and after neck growth. Representative contours of volumetric thermal power dissipation, obtained from FEA of the multilayered unsintered nanoparticle ensemble in Figure 2.4c, are shown at the maximum cross-sectional diameter for each nanoparticle layer in Figure 3.8b.



(a)



(b)

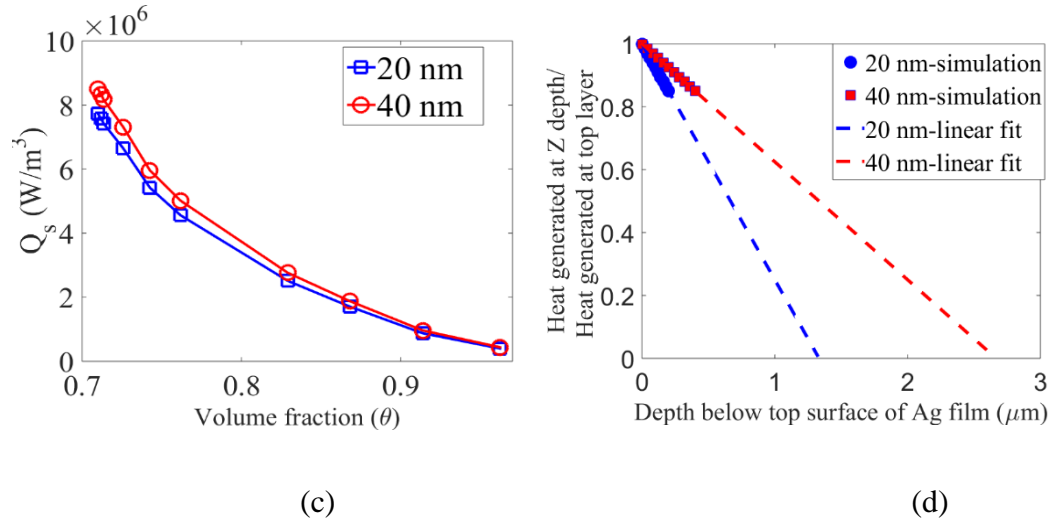
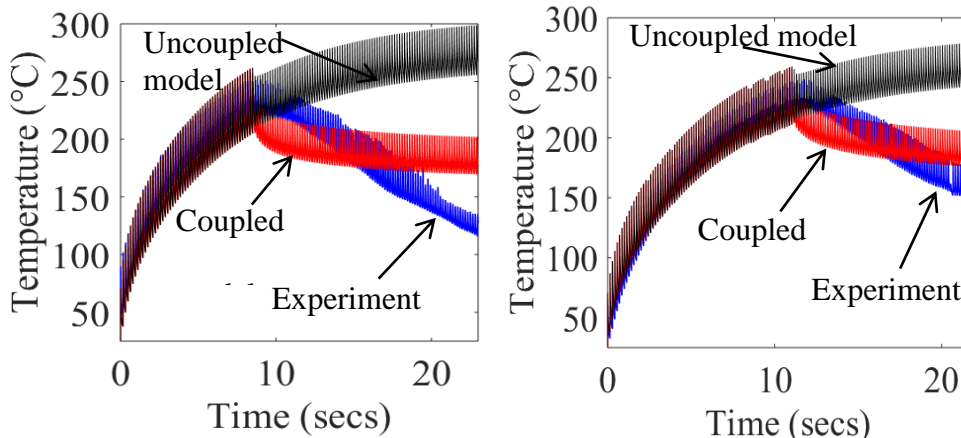


Figure 3.8: (a) Representative predicted contours of volumetric thermal power dissipation in W/m^3 as a function of neck size x , for 20 nm Ag nanoparticles at $\lambda = 400$ nm; (b) Representative predicted contours of volumetric thermal power dissipation in W/m^3 for multilayered unsintered nanoparticle ensemble of 20 nm Ag nanoparticles, at $\lambda = 400$ nm; (c) Predicted function $Q_s(\theta)$; (d) Predicted function $Q_s(z)$. All results shown for 1 V/m incident electric field.

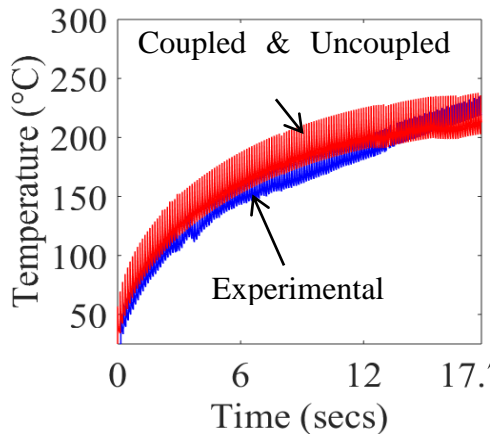
As expected the volumetric power dissipation reduces with increasing depth into the film. Figure 3.8a and Figure 3.8d show the calculated $Q_s(\theta)$ and $Q_s(z)$ respectively. Note that the volumetric thermal power reduces as interparticle necking and solid volume fraction increases (Figure 3.8c). Figure 3.9 and Figure 3.10 compare the evolution of film temperature, as predicted by the coupled and uncoupled mesoscale models, to the experimentally measured temperature evolution. Note that the parameters of the MSC in (11) were calibrated against experimental temperature measurements for fluence E2, for both 20 nm and 40 nm diameter nanoparticles. These calibrated parameters were not changed with fluence or number of pulses during IPL. The greater rise in film temperature per pulse with increasing fluence, for a constant nanoparticle size, is captured by both the coupled and uncoupled models. However, the coupled model captures the experimentally

observed turning point and the subsequent reduction in film temperature with fluence E2 and E3 for both 20 nm (Figure 3.9a, b) and 40 nm nanoparticle films (Figure 3.10a, b), whereas the uncoupled model is unable to do so. The coupled model also captures the experimental observation that the turning point temperature is not reached for fluence E1 (Figure 3.9c and Figure 3.10c). Predictions from the uncoupled model for fluence E1 are not shown here since θ was predicted to be always equal to 0.71 by the coupled model, i.e., no sintering happened. As the predicted temperature rise for $\theta = 0.71$ is the same for the coupled and uncoupled models and the evolution of θ is dependent on the temperature and time, the coupled and uncoupled models will predict identical temperature evolution and no change in volume fraction for fluence E1

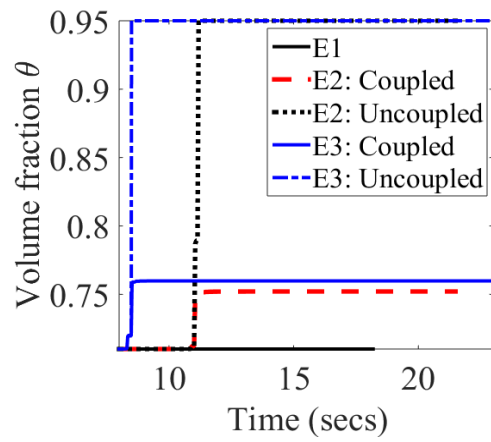


(a)

(b)

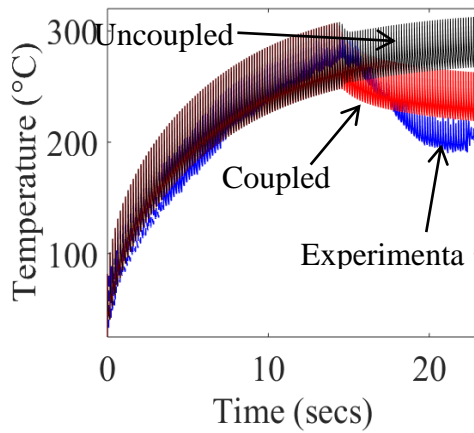


(c)

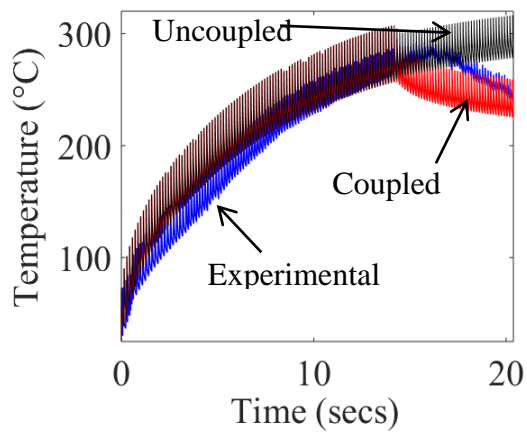


(d)

Figure 3.9: Temperature predictions by coupled and uncoupled models compared to experimentally measured temperature for fluence (a) E3 (b) E2 (c) E1; and (d) Predicted volume fraction, for 20 nm Ag nanoparticle film.



(a)



(b)

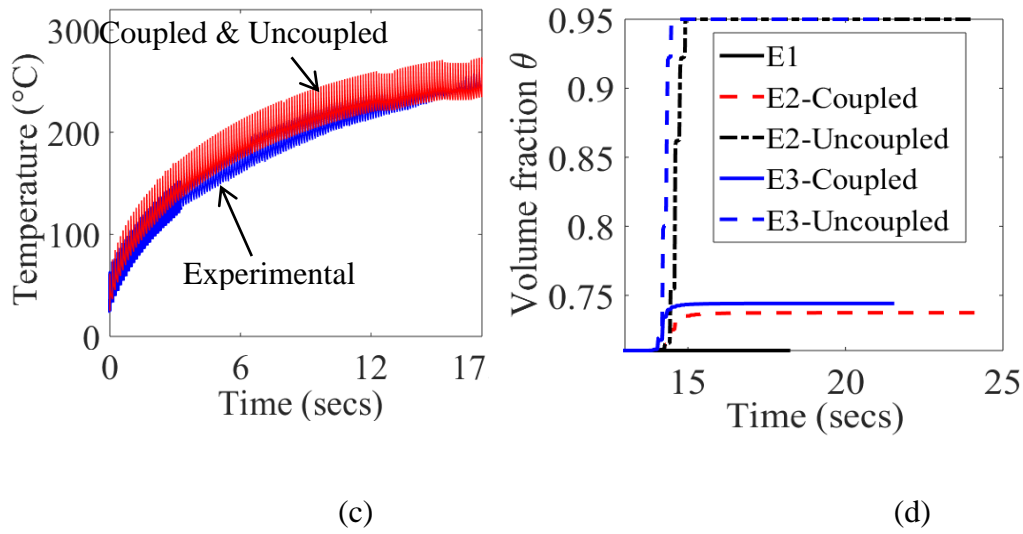


Figure 3.10: Temperature predictions by coupled and uncoupled models compared to experimentally measured temperature for fluence (a) E3 (b) E2 (c) E1; and (d) Predicted volume fraction, for 40 nm Ag nanoparticle film.

The uncoupled model shows a leveling off in densification with increasing number of pulses, as it predicts that full density is reached for fluence E2 and E3. On the other hand, the coupled model predicts a leveling off in densification even when full density has not been reached. Both the models capture the experimental observations that densification occurs faster for fluence E3 than for fluence E2. The coupled model also captures the experimental observation that the sintered density after 150 pulses is greatest for fluence E3. On the other hand, the uncoupled model predicts that both fluence E2 and E3 result in the same sintered density after 150 pulses and also predicts a much higher density than the coupled model. While it is clear that the coupled model is significantly better than the uncoupled model at capturing the temperature evolution during IPL, the question is, is the coupled model also better at capturing the evolution of density during IPL?

In the absence of external pressure, as in IPL, densification depends primarily on the temperature history imposed by the sintering process[62] and the inherent densification characteristics of the deposited nanoparticles. The densification characteristics can be represented by a MSC for a given nanoparticle size, material and packing technique. Note that in this work the MSC for a given nanoparticle size was fixed, based on the calibration method described in section 2.2.2. Therefore, since the evolution of film temperature during IPL is captured much better by the coupled model we contend that the coupled model also prevents the overestimation of densification during IPL by the conventional uncoupled model. The only fundamental difference in the formulation of the coupled and the uncoupled models is that the uncoupled model does not account for the change in optical absorption due to interparticle neck growth during IPL. Since the coupled model captures temperature turning point and density evolution better than the uncoupled model, it is the change in optical absorption due to interparticle necking that causes the turning point in temperature evolution during IPL. A key consequence of this phenomenon is that inline monitoring of temperature evolution to detect the temperature turning point during IPL can be used to identify the onset of film densification and thus enhance inline control of the process. Note that the absence of an experimentally observed temperature turning point for fluence E1 is also captured by the coupled model. This absence of a temperature turning point for fluence E1 is because the minimum energy required for appreciable sintering of the nanoparticles is not reached within 150 pulses for fluence E1. Since the activation energy for sintering is not supplied interparticle neck growth is not appreciable, there is little associated reduction in optical absorption and therefore no temperature turning point for fluence E1. This is further indicated by the fact that the predicted and

experimentally observed temperature for fluence E1 stays below the typical turning point temperature for each nanoparticle film ($\approx 250^\circ\text{C}$ for 20 nm film and $\approx 290^\circ\text{C}$ for 40 nm film). SEM, XRD and conductivity analysis in Figs. 5-7 also show significantly lesser interparticle necking for fluence E1 than for E2 and E3. For fluence E2 and E3 the fluence per pulse is high enough that the activation energy for sintering is supplied within the 150 pulses used here. As a result, there is appreciable interparticle neck growth (Figure 3.2, Figure 3.3, Figure 3.7) to create a reduction in optical absorption and therefore cause a temperature turning point.

It is worth noting that after the temperature turning point the film temperature predicted by the coupled model reduces and reaches a steady state much faster than the experimentally observed temperature, which continues to steadily reduce after the temperature turning point. This is probably because the coupled or uncoupled models do not account for the wide distribution in nanoparticle size seen in Figure 2.1a-b. In a film with a wide distribution of nanoparticle sizes the smaller particles will coalesce with the large ones first to increase particle size [55], followed by neck growth between the now even larger particles. The increase in volume fraction and the reduction in the optically induced heat generation capacity, and therefore the consequent drop in film temperature after the temperature turning point, will therefore be more gradual for a wider distribution in nanoparticle size. On the other hand, since the developed coupled model assumes a very narrow nanoparticle size distribution the loss in optically induced heat generation capacity is very abrupt.

Nonetheless, by capturing the temperature turning point and the drop in temperature after the turning point this coupled model still captures the physics of IPL better than

conventional uncoupled model. The coupled model was further used to parametrically examine the effect of fluence and number of pulses on densification and temperature rise in the Ag film. The pulse on-time was changed while keeping the lamp voltage constant, to change fluence, while ensuring that the minimum off-time required for every combination of on-time and lamp voltage was retained. This minimum off-time corresponds to the capacitor charging time for the Sinteron 3000 flash-lamp system. The simulations were stopped when no further increase in volume fraction was predicted during the simulations.

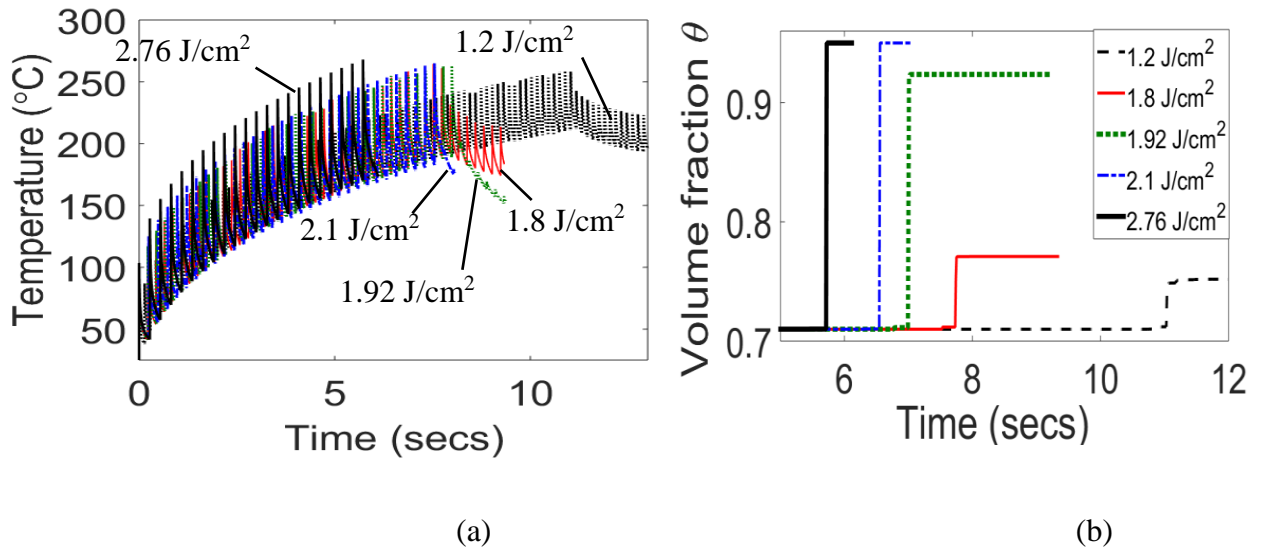


Figure 3.11: Effect of varying fluence and number of pulses on predicted (a) film temperature (b) solid volume fraction, for 20 nm Ag nanoparticle film.

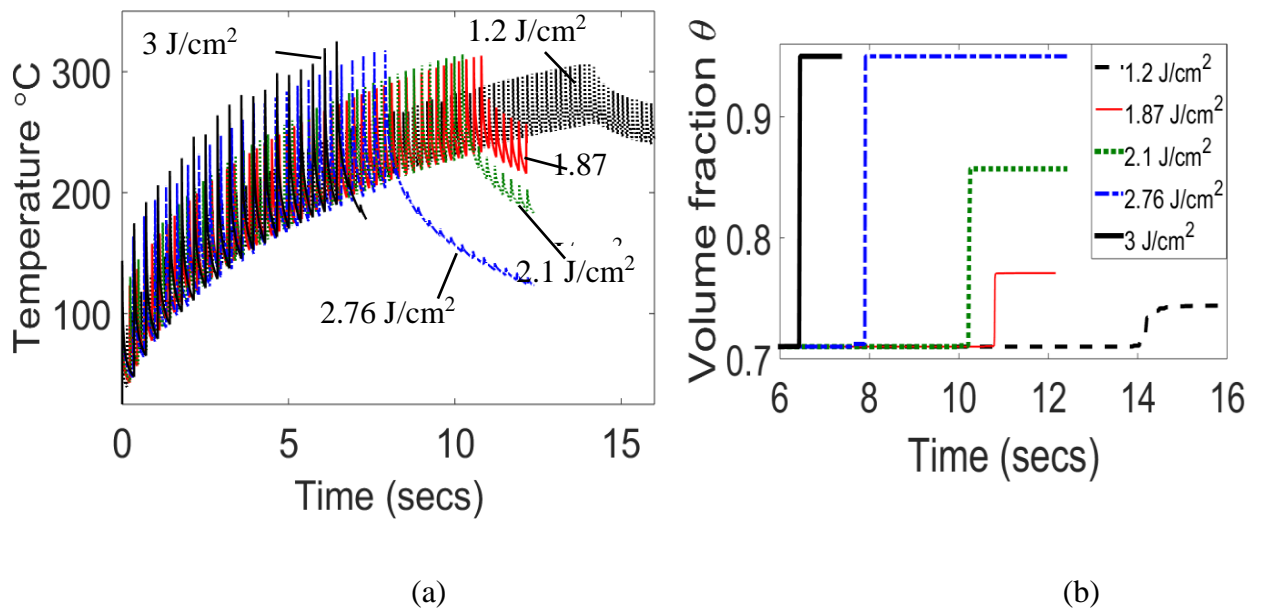


Figure 3.12: Effect of varying fluence and number of pulses on predicted (a) film temperature (b) solid volume fraction, for 40 nm Ag nanoparticle film.

It can be seen that greater fluence results in an increase in temperature per pulse (Figure 3.11a, Figure 3.12a) and faster onset of sintering (Figure 3.11b, Figure 3.12b), which mirrors experimental observations in literature [6, 11]. Furthermore, near full densification can occur without the occurrence of melting of nanoparticles in the film. Figure 3.11b, and Figure 3.12b also show that there is a maximum achievable density corresponding to a given fluence, which is independent of the number of pulses used beyond the temperature turning point. This prediction is in line with the experimental observation [2, 6, 11] that for a fixed fluence the densification levels off after a critical number of pulses. This leveling off in densification occurs because beyond the number of pulses corresponding to the temperature turning point there is a reduction in the optical absorption capacity of the film. The reduction in optical absorption capacity is related to

the growth of interparticle necks at the onset of densification in IPL, and to the coupling between optical absorption and interparticle neck growth seen in figure 8. This in turn reduces the film temperature (Figure 3.11a and Figure 3.12a) and results in a leveling off in densification (Figure 3.11b and Figure 3.12b). Figure 3.11b and Figure 3.12b also show that an increase in fluence increases the above maximum achievable density. This is because despite the reduction in optical absorption capacity at the onset of sintering the higher fluence is still able to drive the absolute magnitude of temperature to levels high enough for additional densification for a while beyond the temperature turning point. This observation also indicates that the fluence exerts a greater influence on the maximum achievable densification in IPL, as compared to the number of pulses. At the same time, combinations of lower fluences and greater number of pulses can also be used to effect greater control of the density of the sintered nanoparticle film in IPL.

4 Conclusions and Future work

In conclusion, this work shows a turning point in the evolution of film temperature during IPL of Ag nanoparticle films, and correlates this turning point in temperature to the onset of densification as well as the change in conductivity of the film. It is shown that the rate of densification reduces after this turning point temperature due to a drop in film temperature. Also, this means that additional microcracking of the film after the temperature turning point might be attributed to thermal shock induced stresses rather than densification induced stresses. A mesoscale thermal-densification model is developed, informed by nanoscale simulations that couple optical absorption and interparticle necking. This model needs just three MSC parameters in (11) to be calibrated and does not need to use the conservative nanoparticle melting criterion as an indicator of densification in the film. Instead, the transient evolution of solid volume fraction during IPL is explicitly modeled. Despite significant assumptions including idealized and non-random nanoparticle packing in the film, monodisperse nanoparticle size distribution and approximation of heat transfer in the film as one-dimensional in nature, this coupled model is able to capture the turning point in temperature during IPL whereas the conventional uncoupled model is unable to do so. At the same time, this coupled model is also able to capture additional experimental effects seen in this work and in literature including the effect of fluence per pulse, number of pulses and nanoparticle size on the evolution of temperature and densification during IPL. Key insights that can be gathered from this work are as follows:

- (1) Increasing number of pulses beyond the temperature turning point has little effect on increasing the densification and conductivity of the film, since the temperature drops due to reduction in optical absorption upon significant interparticle neck growth, while having the detrimental effect of increasing processing time as well as microcracking. This observation of a turning point in temperature and its correlation to densification creates the possibility of identifying the onset of film densification during IPL via inline monitoring of film temperature during IPL. This can enhance inline control of the IPL process to minimize processing time while maximizing function of the film.
- (2) It is shown that accounting for the coupling between optical absorption by the nanoparticle film and densification in the nanoparticle film is critical to explaining the occurrence of the turning point in temperature during IPL, which occurs despite no reduction in pulse energy from the xenon lamp. Since densification in IPL is primarily controlled by film temperature, the above coupling effect also explains the levelling off in densification beyond a critical number of pulses corresponding to the temperature turning point in IPL.
- (3) The dependence of the maximum achievable film density in IPL on the process parameters, shown in Figure 3.11 and Figure 3.12, indicates that the combination of fluence and number of pulses needs to be carefully considered in order to ensure that the required film density is obtained. It is recommended that lesser number of high fluence pulses be used to rapidly obtain high film density, whereas larger number of low fluence pulses be used to retain greater control of sintered film density. This insight further enhances a-priori control of the IPL process.

The coupled model developed here improves the capability to capture the physics of IPL as compared to conventional uncoupled models, but it still does not accurately capture the evolution of film temperature after the temperature turning point. While the coupled model provides an improved prediction of densification as compared to the uncoupled model, it is likely that the faster drop in film temperature after the turning point also results in a slightly underpredicted density. Accounting for the nanoparticle size distribution, and the resultant effects on random nanoparticle packing structure and optical absorption, to resolve this issue can be under the scope of future work.

Bibliography

- [1] K.D. Harris, A.L. Elias, H.J. Chung, Flexible electronics under strain: a review of mechanical characterization and durability enhancement strategies, *J. Mater. Sci.* 51 (2016) 2771–2805. doi:10.1007/s10853-015-9643-3.
- [2] M.-G. Kang, W.-S. Jung, C.-Y. Kang, S.-J. Yoon, Recent Progress on PZT Based Piezoelectric Energy Harvesting Technologies, *Actuators*. 5 (2016) 5. doi:10.3390/act5010005.
- [3] Z. Bi, O. Anderoglu, X. Zhang, J.L. MacManus-Driscoll, H. Yang, Q. Jia, H. Wang, Nanoporous thin films with controllable nanopores processed from vertically aligned nanocomposites., *Nanotechnology*. 21 (2010) 285606. doi:10.1088/0957-4484/21/28/285606.
- [4] S. Norita, D. Kumaki, Y. Kobayashi, T. Sato, K. Fukuda, S. Tokito, Inkjet-printed copper electrodes using photonic sintering and their application to organic thin-film transistors, *Org. Electron*. 25 (2015) 131–134. doi:10.1016/j.orgel.2015.06.026.
- [5] V. Sanchez-Romaguera, S. Wünscher, B.M. Turki, R. Abbel, S. Barbosa, D.J. Tate, D. Oyeka, J.C. Batchelor, E. a. Parker, U.S. Schubert, S.G. Yeates, Inkjet printed paper based frequency selective surfaces and skin mounted RFID tags: the interrelation between silver nanoparticle ink, paper substrate and low temperature sintering technique, *J. Mater. Chem. C*. 3 (2015) 2132–2140. doi:10.1039/C4TC02693D.
- [6] S. Han, Y. Zhou, V.A.L. Roy, Towards the Development of Flexible Non-Volatile

- Memories, (2013) 5425–5449. doi:10.1002/adma.201301361.
- [7] W.H. and H.Z. Chaoliang Tan, Zhengdong Liu, Non-volatile resistive memory devices based on solution-processed ultrathin two-dimensional nanomaterials, *Chem. Soc. Rev.* 44 (2015) 2615–2628. doi:10.1039/C4CS00399C.
- [8] and K.C.C. Sung-Min Lee, Jeong Hyun Kwon, Seonil Kwon, A Review of Flexible OLEDs Toward Highly Durable Unusual Displays, *XX* (2017) 1–10.
- [9] T.D. Lee, A.U. Ebong, A review of thin film solar cell technologies and challenges, *Renew. Sustain. Energy Rev.* 70 (2016) 1286–1297. doi:10.1016/j.rser.2016.12.028.
- [10] M.R. Somalu, A. Muchtar, W. Ramli, W. Daud, N.P. Brandon, Screen-printing inks for the fabrication of solid oxide fuel cell films : A review, *Renew. Sustain. Energy Rev.* (2016) 0–1. doi:10.1016/j.rser.2016.11.008.
- [11] L. Li, Z. Wu, S. Yuan, X.-B.B. Zhang, Advances and challenges for flexible energy storage and conversion devices and systems, *Energy Environ. Sci.* 7 (2014) 2101. doi:10.1039/c4ee00318g.
- [12] M. Zhi, C. Xiang, J. Li, M. Li, N. Wu, Nanostructured carbon – metal oxide composite electrodes for supercapacitors : a review, (2013) 72–88. doi:10.1039/c2nr32040a.
- [13] C.W. and Y.X. Xu Peng, Lele Peng, Two dimensional nanomaterials for flexible supercapacitors, *Chem. Soc. Rev.* 43 (2014) 3303–3323. doi:10.1039/c3cs60407a.
- [14] M. Shi, H. Wu, J. Zhang, M. Han, B. Meng, H. Zhang, Nano Energy Self-powered wireless smart patch for healthcare monitoring, *Nano Energy.* 32 (2017) 479–487.

doi:10.1016/j.nanoen.2017.01.008.

- [15] A. Nag, S. Chandra, J. Kosel, *Sensors and Actuators A : Physical Flexible carbon nanotube nanocomposite sensor for multiple physiological parameter monitoring*, *Sensors Actuators A. Phys.* 251 (2016) 148–155. doi:10.1016/j.sna.2016.10.023.
- [16] A. Kaushik, R. Kumar, S.K. Arya, M. Nair, B.D. Malhotra, S. Bhansali, *Organic – Inorganic Hybrid Nanocomposite-Based Gas Sensors for Environmental Monitoring*, (2015). doi:10.1021/cr400659h.
- [17] P. Innocenzi, L. Malfatti, *Mesoporous thin films: properties and applications.*, *Chem. Soc. Rev.* 42 (2013) 4198–216. doi:10.1039/c3cs35377j.
- [18] Y.-F. Sun, S.-B. Liu, F.-L. Meng, J.-Y. Liu, Z. Jin, L.-T. Kong, J.-H. Liu, *Metal Oxide Nanostructures and Their Gas Sensing Properties: A Review*, *Sensors.* 12 (2012) 2610–2631. doi:10.3390/s120302610.
- [19] A. Gupta, J.R. Saurav, S. Bhattacharya, *Solar light based degradation of organic pollutants using ZnO nanobrushes for water filtration*, *RSC Adv.* 5 (2015) 71472–71481. doi:10.1039/C5RA10456D.
- [20] F. Han, G. Meng, F. Zhou, L. Song, X. Li, X. Hu, X. Zhu, B. Wu, B. Wei, *Dielectric capacitors with three-dimensional nanoscale interdigital electrodes for energy storage.*, *Sci. Adv.* 1 (2015) e1500605. doi:10.1126/sciadv.1500605.
- [21] A. Kamyshny, S. Magdassi, *Conductive nanomaterials for printed electronics*, *Small.* 10 (2014) 3515–3535. doi:10.1002/sml.201303000.
- [22] P.P. Boix, K. Nonomura, N. Mathews, S.G. Mhaisalkar, *Current progress and future*

- perspectives for organic/inorganic perovskite solar cells, *Mater. Today*. 17 (2014) 16–23. doi:10.1016/j.mattod.2013.12.002.
- [23] N. Ali, A. Hussain, R. Ahmed, M.K. Wang, C. Zhao, B.U. Haq, Y.Q. Fu, Advances in nanostructured thin film materials for solar cell applications, *Renew. Sustain. Energy Rev.* 59 (2016) 726–737. doi:10.1016/j.rser.2015.12.268.
- [24] T.D. Lee, A.U. Ebong, A review of thin film solar cell technologies and challenges, *Renew. Sustain. Energy Rev.* 70 (2017) 1286–1297. doi:10.1016/j.rser.2016.12.028.
- [25] X. Yu, T.J. Marks, A. Facchetti, Metal oxides for optoelectronic applications, *Nat. Mater.* 15 (2016) 383–396. doi:10.1038/nmat4599.
- [26] T. Seifert, E. Sowade, F. Roscher, M. Wiemer, T. Gessner, R.R. Baumann, Additive manufacturing technologies compared: Morphology of deposits of silver ink using inkjet and aerosol jet printing, *Ind. Eng. Chem. Res.* 54 (2015) 769–779. doi:10.1021/ie503636c.
- [27] J. Perelaer, U.S. Schubert, Novel approaches for low temperature sintering of inkjet-printed inorganic nanoparticles for roll-to-roll (R2R) applications, *J. Mater. Res.* 28 (2013) 564–573. doi:10.1557/jmr.2012.419.
- [28] P. Peng, A. Hu, A.P. Gerlich, G. Zou, L. Liu, Y.N. Zhou, Joining of Silver Nanomaterials at Low Temperatures: Processes, Properties, and Applications, *ACS Appl. Mater. Interfaces.* 7 (2015) 12597–12618. doi:10.1021/acsami.5b02134.
- [29] J. Perelaer, B.J. De Gans, U.S. Schubert, Ink-jet printing and microwave sintering of conductive silver tracks, *Adv. Mater.* 18 (2006) 2101–2104.

doi:10.1002/adma.200502422.

- [30] H. Lee, D. Kim, I. Lee, Y.J. Moon, J.Y. Hwang, K. Park, S.J. Moon, Stepwise current electrical sintering method for inkjet-printed conductive ink, *Jpn. J. Appl. Phys.* 53 (2014). doi:10.7567/JJAP.53.05HC07.
- [31] S. Ma, V. Bromberg, L. Liu, F.D. Egitto, P.R. Chiarot, T.J. Singler, Low temperature plasma sintering of silver nanoparticles, *Appl. Surf. Sci.* 293 (2014) 207–215. doi:10.1016/j.apsusc.2013.12.135.
- [32] S.S. Yoon, D.Y. Khang, Room-Temperature Chemical Welding and Sintering of Metallic Nanostructures by Capillary Condensation, *Nano Lett.* 16 (2016) 3550–3556. doi:10.1021/acs.nanolett.6b00621.
- [33] H.-J. Hwang, K.-H. Oh, H.-S. Kim, All-photonic drying and sintering process via flash white light combined with deep-UV and near-infrared irradiation for highly conductive copper nano-ink., *Sci. Rep.* 6 (2016) 19696. doi:10.1038/srep19696.
- [34] S. Wünscher, R. Abbel, J. Perelaer, U.S. Schubert, Progress of alternative sintering approaches of inkjet-printed metal inks and their application for manufacturing of flexible electronic devices, *J. Mater. Chem. C.* 2 (2014) 10232–10261. doi:10.1039/C4TC01820F.
- [35] J. Niittynen, R. Abbel, M. Mäntysalo, J. Perelaer, U.S. Schubert, D. Lupo, Alternative sintering methods compared to conventional thermal sintering for inkjet printed silver nanoparticle ink, *Thin Solid Films.* 556 (2014) 452–459. doi:10.1016/j.tsf.2014.02.001.

- [36] J. Niittynen, E. Sowade, H. Kang, R.R. Baumann, M. Mäntysalo, Comparison of laser and intense pulsed light sintering (IPL) for inkjet-printed copper nanoparticle layers., *Sci. Rep.* 5 (2015) 8832. doi:10.1038/srep08832.
- [37] Y. Galagan, E.W.C. Coenen, R. Abbel, T.J. van Lammeren, S. Sabik, M. Barink, E.R. Meinders, R. Andriessen, P.W.M. Blom, Photonic sintering of inkjet printed current collecting grids for organic solar cell applications, *Org. Electron.* 14 (2013) 38–46. doi:10.1016/j.orgel.2012.10.012.
- [38] H.S. Kim, S.R. Dhage, D.E. Shim, H.T. Hahn, Intense pulsed light sintering of copper nanoink for printed electronics, *Appl. Phys. A Mater. Sci. Process.* 97 (2009) 791–798. doi:10.1007/s00339-009-5360-6.
- [39] M. Jha, R. Dharmadasa, G.L. Draper, a Sherehiy, G. Sumanasekera, D. Amos, T. Druffel, Solution phase synthesis and intense pulsed light sintering and reduction of a copper oxide ink with an encapsulating nickel oxide barrier, *Nanotechnology.* 26 (2015) 175601. doi:10.1088/0957-4484/26/17/175601.
- [40] J.S. Kang, J. Ryu, H.S. Kim, H.T. Hahn, Sintering of inkjet-printed silver nanoparticles at room temperature using intense pulsed light, *J. Electron. Mater.* 40 (2011) 2268–2277. doi:10.1007/s11664-011-1711-0.
- [41] H.-J. Hwang, W.-H. Chung, H.-S. Kim, *In situ* monitoring of flash-light sintering of copper nanoparticle ink for printed electronics, *Nanotechnology.* 23 (2012) 485205. doi:10.1088/0957-4484/23/48/485205.
- [42] W. Macneill, C. Choi, C. Chang, R. Malhotra, On the self-damping nature of densification in photonic sintering of nanoparticles, *Nat. Publ. Gr.* 5 (2015) 1–13.

doi:10.1038/srep14845.

- [43] S.H. Park, H.S. Kim, Flash light sintering of nickel nanoparticles for printed electronics, *Thin Solid Films*. 550 (2014) 575–581. doi:10.1016/j.tsf.2013.11.075.
- [44] S.R. Dhage, H.T. Hahn, Journal of Physics and Chemistry of Solids Rapid treatment of CIGS particles by intense pulsed light, *J. Phys. Chem. Solids*. 71 (2010) 1480–1483. doi:10.1016/j.jpcs.2010.07.016.
- [45] R. Dharmadasa, B. Lavery, I.M. Dharmadasa, T. Dru, Intense Pulsed Light Treatment of Cadmium Telluride Nanoparticle- Based Thin Films, (2014).
- [46] B.A. Williams, M.A. Smeaton, C.S. Holgate, L.F. Francis, E.S. Aydil, Effect of intense pulsed light annealing on the microstructure of copper zinc tin sulfide nanocrystal coatings, 4 (2015) 1–28. doi:10.1116/1.4961661.
- [47] G. Palermo, R. Caputo, A. De Luca, C.P. Umeton, Control of the optically induced heating of gold nanoparticles, *Photonics Lett. Pol.* 9 (2017) 17. doi:10.4302/plp.v9i1.706.
- [48] G. Baffou, R. Quidant, Thermo-plasmonics: Using metallic nanostructures as nano-sources of heat, *Laser Photonics Rev.* 7 (2013) 171–187. doi:10.1002/lpor.201200003.
- [49] D.J. Lee, S.H. Park, S. Jang, H.S. Kim, J.H. Oh, Y.W. Song, Pulsed light sintering characteristics of inkjet-printed nanosilver films on a polymer substrate, *J. Micromechanics Microengineering*. 21 (2011) 125023. doi:10.1088/0960-1317/21/12/125023.

- [50] J. West, M. Carter, S. Smith, J. Sears, Photonic Sintering of Silver Nanoparticles : Comparison of Experiment and Theory, InTech, 2012.
- [51] B.W. Lavery, S. Kumari, H. Konermann, G.L. Draper, J. Spurgeon, T. Druffel, Intense Pulsed Light Sintering of CH₃NH₃PbI₃ Solar Cells, ACS Appl. Mater. Interfaces. 8 (2016) 8419–8426. doi:10.1021/acsami.5b10166.
- [52] S.H. Park, W.H. Chung, H.S. Kim, Temperature changes of copper nanoparticle ink during flash light sintering, J. Mater. Process. Technol. 214 (2014) 2730–2738. doi:10.1016/j.jmatprotec.2014.06.007.
- [53] S. Bansal, R. Malhotra, Nanoscale-shape-mediated coupling between temperature and densification in intense pulsed light sintering, Nanotechnology. 27 (2016) 495602. doi:10.1088/0957-4484/27/49/495602.
- [54] X. Fan, W. Zheng, D.J. Singh, Light scattering and surface plasmons on small spherical particles, Light Sci. Appl. 3 (2014) e179. doi:10.1038/lsa.2014.60.
- [55] F. Parhami, R.M. McMeeking, a. C.F. Cocks, Z. Suo, A model for the sintering and coarsening of rows of spherical particles, Mech. Mater. 31 (1999) 43–61. doi:10.1016/S0167-6636(98)00049-0.
- [56] K.K. Nanda, A. Maisels, F.E. Kruis, H. Fissan, S. Stappert, Higher Surface Energy of Free Nanoparticles, Phys. Rev. Lett. 91 (2003) 106102–1. doi:10.1103/PhysRevLett.92.179601.
- [57] J. Kucera, Self-diffusion in polycrystalline silver, Czechoslov. J. Phys. 14 (1964) 915–922. doi:10.1016/j.cocis.2010.05.014.

- [58] C.N. Singman, Atomic volume and allotropy of the elements, *J. Chem. Educ.* 61 (1984) 137. doi:10.1021/ed061p137.
- [59] L. Gunnarsson, T. Rindzevicius, J. Prikulis, B. Kasemo, M. Ka, S. Zou, G.C. Schatz, Confined Plasmons in Nanofabricated Single Silver Particle Pairs : Experimental Observations of Strong Interparticle Interactions, *J. Phys. Chem. B.* 109 (2005) 1079–1087.
- [60] K.L. Kelly, E. Coronado, L.L. Zhao, G.C. Schatz, The Optical Properties of Metal Nanoparticles: The Influence of Size, Shape, and Dielectric Environment, *J. Phys. Chem. B.* 107 (2003) 668–677.
- [61] D. Nield, A. Bejan, *Convection in Porous Media Third Edition*, 2006. <http://www.springerlink.com/content/x30210/#section=471823&page=1>.
- [62] H.S. and D.L. Johnson, *Master Sintering Curve: A practical approach to Sintering*, *J. Am. Ceram. Soc.* 12 (1996) 3211–17.
- [63] A.O. Govorov, W. Zhang, T. Skeini, H. Richardson, J. Lee, N.A. Kotov, Gold nanoparticle ensembles as heaters and actuators: Melting and collective plasmon resonances, *Nanoscale Res. Lett.* 1 (2006) 84–90. doi:10.1007/s11671-006-9015-7.
- [64] H. a. Alarifi, M. Atiş, C. Özdoğan, a. Hu, M. Yavuz, Y. Zhou, Determination of complete melting and surface premelting points of silver nanoparticles by molecular dynamics simulation, *J. Phys. Chem. C.* 117 (2013) 12289–12298. doi:10.1021/jp311541c.
- [65] J.-M. Lebrun, S.K. Jha, K.S. Naik, K.C. Seymour, W.M. Kriven, R. Raj, *The Change*

of X-ray Diffraction Peak Width During in situ Conventional Sintering of Nanoscale
Powders, *J. Am. Ceram. Soc.* 768 (2016) 765–768. doi:10.1111/jace.14112.